CrystEngComm

Accepted Manuscript

ROYAL SOCIETY OF CHEMISTRY

www.rsc.org/crystengcomm

Mesocrystals as a Class of Multifunctional Materials

Yanqiong Liu,[a] Yu Zhang,[a] John Wang*[a]

[a] Department of Materials Science and Engineering, Faculty of Engineering, National University of Singapore, Singapore 117574 Fax: + (65) 6776-3604; Tel: + (65) 6516-1268; E-mail: msewangj@nus.edu.sg

Abstract

Mesocrystals that consist of crystallographically aligned individual building blocks and controlled level of porosity in between exhibit unique structures and multifunctional behavior. A large number of mesocrystals have been successfully developed by different growth technologies, and various growth mechanisms are discussed. In addition to various self-assembly and growth techniques, considerable attention has been paid to the formation mechanisms where the crystalline colloidal nanoparticles are assembled into mesocrystals *via* interparticle forces or physical fields. Owing to their high surface area, controllable level of porosity, crystallinity of subunits, oriented subunit alignment, and elegant 3D network structure, the performance of mesocrystals can precede their nanocrystalline, single-crystal, and polycrystalline counterparts. There has been a surge in the number of applications demonstrated for mesocrystals over the past couple of years, showing their great application potentials.

1. Introduction

Mesocrystal, as an abbreviation for *mesoscopically structured crystal*, represents a structure composed of nanocrystal subunits aligned in a crystallographic pattern but separated by porosity or a second phase. The first observation of mesocrystal dates back to 1969 when Petres *et al.* deduced a porous intermediate structure of $BaSO_4$.[1] In 2003, Cölfen and Mann stated that *mesoscale assembly* of nanocrystals contributed another mechanism for growing single crystals.[2] In such a mesoscale assembly process, the crystalline primary nanoparticles are aligned in all crystallographic directions to form *"iso-oriented"* crystals. This is in sharp contrast to the *classical crystallization* process whereby the crystallized primary nanoparticles grow *via* ion-by-ion attachment to achieve an amplified single crystal. In 2005, Cölfen and Antonietti coined the word *mesocrystal* as a replacement for "iso-oriented" crystals and proposed that mesocrystals are kinetically metastable intermediates, of which the primary units can still be identified.[3] In a *nonclassical* crystallization reaction process, these mesocrystals transform to single crystals with typical defects. This is a kinetic control of crystallization based on predominantly the splitting of the activation energy barrier such that the whole process proceeds stepwise with smaller activation energy barriers.[2] In 2010, Song and Cölfen contributed a preciser definition that mesocrystals are superstructured crystals consisting of mesoscopically scaled (1-1000 nm) crystalline subunits that are

aligned in a crystallogrpahic register.[4] The mutual order of the subunits may impose difficulty in distinguishing a mesocrystal from a single crystal due to their identical behavioral responses to many characterization techniques, for example, transmission electron microscopy (TEM) diffraction and polarized light.[3, 5, 6] The coherence length in scattering obtainable from X-ray Diffraction (XRD) may be used to set up the borderline between mesocrystals and single crystals. The coherence length of single crystals is usually bigger than 100 nm, while that of mesocrystals is typically smaller. The *crystalline subunits* in mesocrystals are often interspaced by organic additives, pores, or a second phase such as amorphous matter. This suggests that the microscope imaging could be employed to differentiate between mesocrystals and single crystals. The significant difference between the architectures of mesocrystals and single crystals however reveals that the formation mechanism of mesocrystals is completely different from the classical crystal growth pathway of single crystals.

Over the past 4 years (2010-2013), various types of mesocrystals have been synthesized and they can be categorized according to their chemical composition into metals (*e.g.,* Au,[7] Cu,[8] Ag,[9, 10] and Pd[11]), metal oxides (*e.g.,*CeO_2,[12, 13-16] TiO_2,[17-34] ZnO,[35-53] Fe_2O_3,[54-56] Fe_3O_4,[57] Co_3O_4,[58, 59] CoO,[60] Cu_2O,[61] VO_2,[62] SnO,[63] CuO,[64-66] $W_{18}O_{49}$,[67-69] Ag_2O,[70] Al_2O_3,[71] V_2O_5,[72] and MnO[73]), and complex compounds (*e.g.,*EuF_3,[74] YF_3,[75, 76] NH_4TiOF_3,[77-81] and $NaYF_4$[82], $KNbO_3$,[83]

$LiFePO_4$,[84-88] $CaCO_3$,[89-100] $K_4[Fe(CN)_6]$,[101, 102] $K_3[Fe(CN)_6]$,[103] $LiCoO_2$,[104] YBO_3,[105] $AgIn(WO_4)_2$,[106] $CeOHCO_3$,[15] $CaMoO_4$,[107] $BaCO_3$,[108] CuI,[109] $BaTiO_3$,[110-113] $SrTiO_3$,[114-116] BaSO4,[117, 118] $Fe_{10}O_{14}(OH)_2$,[119] $LiMn_2O_4$,[120] $MnWO_4$,[121] $Co(OH)_2$,[122, 123] $In(OH)_3$,[124] PbS,[125] YPO_4,[126] $ErPO_4$,[126] $Bi_{0.5}Na_{0.5}TiO_3$,[127] and $LnBO_3:Eu^{3+}$(Ln=Y, Tb)[128]).

A few review articles focused on the synthesis and formation mechanisms of mesocrystals are available in literature.[2-4, 129-131] A review that briefly summarizes the properties and potential applications of some mesocrystals was published by Zhou and O'Brien in 2012.[132] The present review addresses the general formation mechanisms of mesocrystals with highlight of the influence of interparticle forces and physical fields on orienting nanocrystals into a crystallographic register. In addition, this review surveys the research development in the performance and applications of mesocrystals between 2010 and 2013, especially featuring the latest research advances since 2012.

2. Formation Mechanisms

Without crystallization, precursor ions condense without periodic arrangements on the atomic scale and form amorphous solids (Figure 1, *precursor ions* -> *amorphous solid*). In contrary, crystallization refers to a process where the atoms are arranged periodically. Crystalline matericals include single crystals, polycrystals and mesocrystals. In single crystals, the atoms are arranged

periodically throughout the whole crystal except some minor random defects. In polycrystals, the patches where the atoms are periodically arranged are not crystallographically aligned. For mesocrystals, these patches are crystallographically aligned but inter-spaced by impurities and defects, *e.g.,* organic occlusions, solvent, amorphous counterparts, voids, *etc*.

Single Crystal. Classically, crystallization starts from clustering of the primary building blocks, such as atoms, ions or molecules. If the cluster reaches a critical size, further growth *via* ion-by-ion attachment will lead to unit cell replication and consequently crystal growth. Otherwise, the nanocrystal will disintegrate, *i.e.*, dissolve back into the solution, and the dissolved ions will contribute to growth of the larger nanocrystals which have reached the critical size. This is a typical Ostwald ripening process where the larger nanocrystals grow at the expenses of the smaller ones driven by the thermodynamic force. This process happens at low supersaturation and results in single crystals (Figure 1, *precursor ions -> nanocrystal -> single crystal*).

Polycrystal. High supersaturation usually gives rise to abundant nanocrystals that are highly unstable due to the high surface/volume ratio. Random aggregation effectively relieves the high surface energy but result in polycrystals without crystallographic alignment (Figure 1, *precursor ions -> nanocrystal -> polycrystal*).

Mesocrystal. Non-classically, crystal growth proceeds typically *via* the

integration of classically crystallized subunits, *i.e.*, the nanocrystals attach to each other in an oriented manner *via* mesoscale assembly. Mesocrystals are resulted with all the consisting nanocrystals crystallographically aligned (Figure 1, *precursor ions -> nanocrystal -> mesocrystal*). In the presence of organic additives, more formation mechanisms and mesocrystal structures are emerging depending on the diverse structures of classically crystallized subunits that are completely covered (Nanocrystal 1 in Figure 2), partially covered (Nanocrystals 2, 3 in Figure 2), or not covered at all (nanocrystals in Figure 1) by organic molecules. Since this process requires rotation of the nanocrystals for oriented attachment, intermediate supersaturation is ideal for mesocrystal formation.

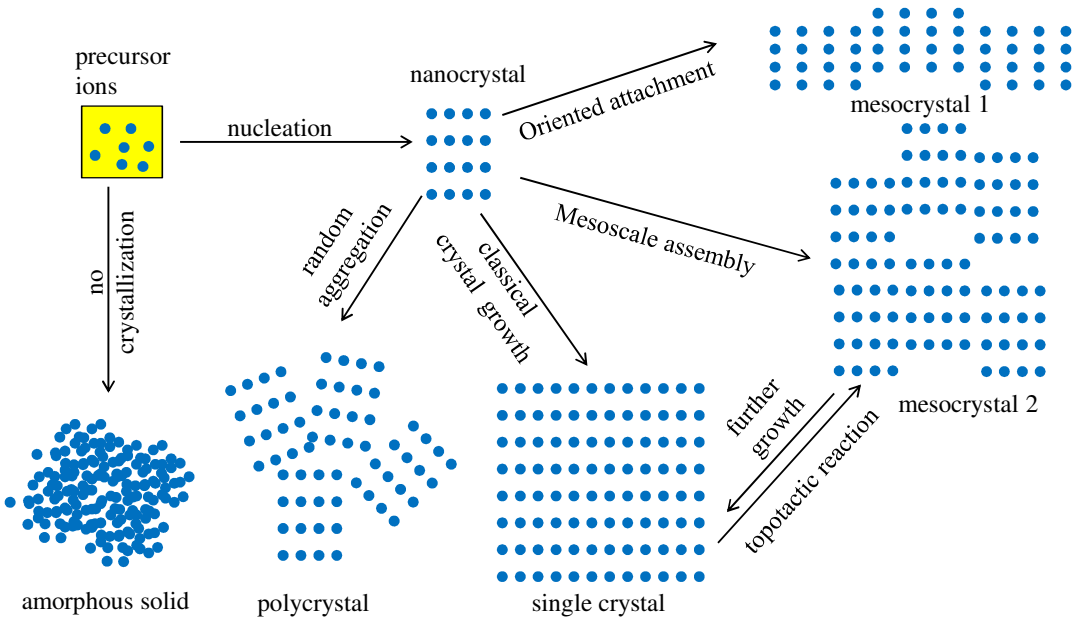

Figure 1. Schematic illustration of different formation mechanisms of various solids in the absence of organic additives.

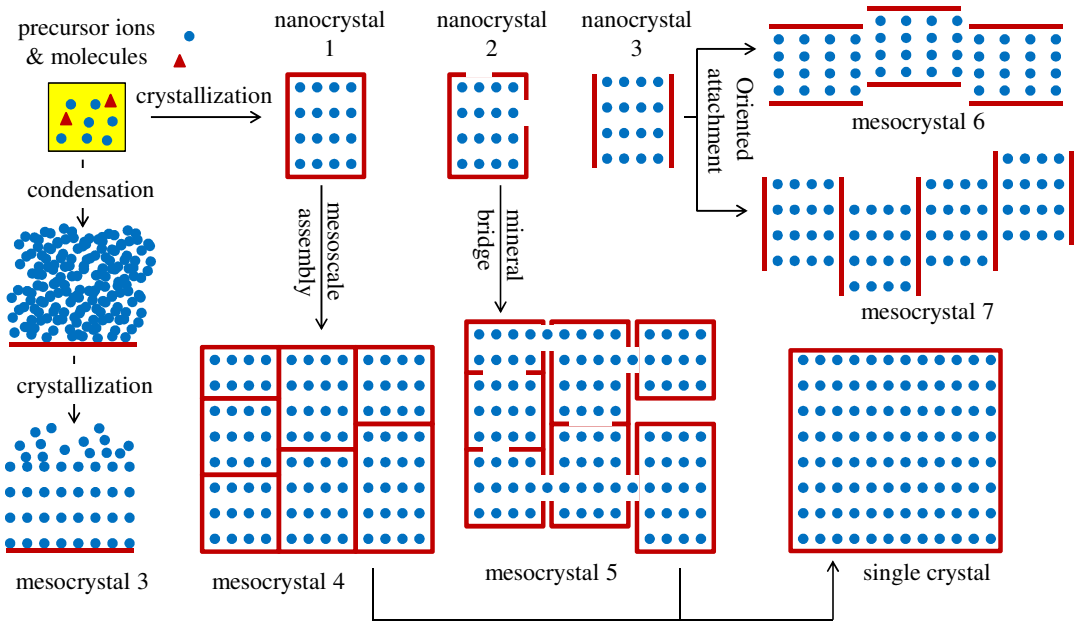

Figure 2. Schematic illustration of different formation mechanisms of various solids in the presence of organic additives.

2.1. Interparticle Forces

In order to realize the directional aggregation of oriented attachment, various mechanisms have been reported. First of all, the strategies for colloidal stabilization shed light on manipulating the interparticle forces among nanocrystals. Interparticle forces existing among nanoparticles in aqueous solutions may include attractive *Van der Waals force* that exists essentially in all materials, repulsive *hydration / solvation force* caused by water or other water-interacting molecules adsorbed on the surfaces, attractive or repulsive *electrostatic force* due to ions on the surfaces, and attractive *hydrophobic force* imposed by hydrophobic polymer chains that are anchored to the particle surfaces. The general colloidal stabilization strategies in aqueous solution include three categories as shown in Figure 3, namely, polymeric

stabilization, electrostatic stabilization, and electrosteric stabilization. Understanding these strategies and the interparticle forces involved will provide insights for modifying them to achieve oriented attachment of nanocrystals in colloidal systems, which is essential to mesocrystal formation.

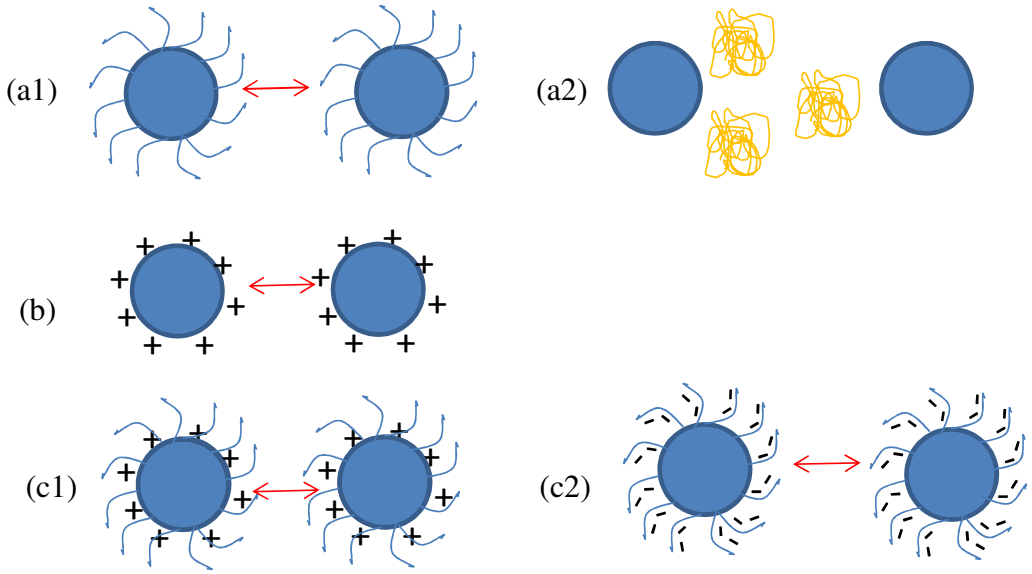

Figure 3. General colloidal stabilization methods in aqueous solution.[133] (a) polymeric stabilization: (a1) steric stabilization, (a2) depletion stabilization; (b) electrostatic stabilization; (c) electrosteric stabilization: (c1) charges and nonionic hydrophilic polymer, (c2) polyelectrolytes. These strategies may be modified to induce oriented attachment for mesocrystal formation. See text for details.

2.1.1. Polymeric Stabilization

Polymeric stabilization for colloidal systems includes two general methods: steric stabilization and depletion stabilization.

Steric stabilization utilizes the steric hindrance of long dangling hydrophilic polymeric chains that are attached to the surfaces of nanocrystals for hindering the

close contacts of neighboring nanocrystals. This process hints that oriented attachment can proceed on the exposed crystallographic surfaces while the other surfaces are stabilized by the selective adsorption of **hydrophilic** polymers. Examples of such polymers are double hydrophilic block copolymers (DHBCs) consisting of a hydrophilic block attached to inorganic minerals and another hydrophilic block that contributes to steric hindrance. Helices of $BaCO_3$ fibers with a diameter in the range of 200-500 nm and lengths as long as a few millimeters were formed in the presence of a DHBC (polyethylene glycol-b-[(2-[4-dihydroxyphosphoryl]-2-oxabutyl) acrylate ethyl ester]).[134] The helical $BaCO_3$ fibers were composed of nanocrystals with a diameter of ~30 nm and length of ~200 nm. The nanocrystals assembled towards helices because of the selective adsorption of the polymers on the (110) face of $BaCO_3$ nanocrystals. Similarly, very thin triangles, truncated triangular nanoprisms, and hexagons of Au were prepared by self-reduction of $HAuCl_4$ in the presence of a DHBC (PEG-b-hexacyclen) because of the specific adsorption of the polymer on (111) faces.[135] This was evidenced by molecular modeling that the span distance of the neighboring $–NH_2$ groups of PEG-b-hexacyclen matches well with the distance of the neighboring Au atoms in the (111) face. This route is shown in Figure 2 *precursor ions & molecules -> nanocrystal 3 -> mesocrystal 6*. This process also hints that selective / preferential adsorption of **hydrophobic** chains anchored to

certain crystallographic surfaces will drive oriented attachment at these surfaces. For example, $BaCrO_4$ chains and 2D superlattices have been prepared utilizing the hydrophobic tails of Barium bis(2-ethylhexyl)sulphosuccinate ($Ba(AOT)_2$) surfactant molecules adsorbed specifically to the side surfaces of prismatic $BaCrO_4$ nanocrystals.[136] The distance in-between two neighboring $BaCrO_4$ nanocrystals was ~2 nm corresponding to the thickness of interdigitated surfactant layer. This route is shown in Figure 2 by *precursor ions & molecules -> nanocrystal 3 -> mesocrystal 7*. Zhou *et al.* proposed that Brij 58 ($C_{16}H_{33}(PEO)_{20}OH$) surfactant molecules adsorbed onto the surfaces of NH_4TiOF_3 nanocrystals *via* the PEO groups and the hydrophobic $C_{16}H_{33}$ groups introduced hydrophobic interaction for mesoscale assembly of the nanocrystals.[137] Since the interaction sites for the PEO groups varied from crystallographic faces to faces, it is suggested the directional self-assemlby could be controlled by the density of surface **hydrophobic** chains. This route is shown in Figure 2 by *precursor ions & molecules -> nanocrystal 1 -> mesocrystal 4*.

Depletion stabilization makes use of the energy barrier that the free macromolecules have to overcome when they move to higher concentration regions to make way for the aggregating nanocrystals. However, when two particles have come so close that the region in between them is free of macromolecules, flocculation of these two particles is more favorable.[138] This stabilization method

suggests that free macromolecules are not favored in the case of oriented attachment since precise control is not feasible.

2.1.2. Electrostatic Stabilization

Electrostatic stabilization operates via the electrostatic repulsion between net surface charges caused by ionization of surface atoms, binding of solution ions, ion exchange between surface and solution. A typical example is cetyltrimethylammonium bromide (CTAB $(C_{16}H_{33})N(CH_3)_3Br$) coated Au nanocrystals that are stabilized by the bilayer structure of CTA^+ ions on the surfaces.[139] In accordance with this method, oriented attachment may be realized via selectively neutralizing some crystallographic faces of the electrostatically stabilized nanocrystals so that assembly can proceed via the neutralized crystallographic faces. For example, 3-mercaptopropionic acid molecules preferentially interdigitate the less dense CTAB bilayer at the ends of Au nanorods and induce their end-to-end assembly at pH 9.6; whereas, 11-mercaptoundecanoic acid molecules can penetrate through the dense CTAB bilayer at the sides of Au nanorods and induce side-to-side assembly of Au nanorods at pH 6.2.[140] Another excellent example is the formation of pearl-like structure of anatase by controlling pH so that isoelectric point (IEP) of a certain crystallographic surface (*i.e.* (001)) is equal to solution pH and oriented attachment may continue via these surfaces.[141] This is shown in Figure 1 by the route *precursor ions -> nanocrystal -> mesocrystal*

1. Oriented attachment may also be possible if the nanocrystals intrinsically consist of alternate layers of positively and negatively charged atoms in one crystallographic direction. A good example is the formation of ZnO nanorods after reflux of the starting sol that is composed of ZnO nanocrystals.[142] The atomic layers perpendicular to *c*-axis alternately consist of Zn^{2+} and O^{2-} ions.[143] This is shown in Figure 1 by the route *precursor ions -> nanocrystal -> mesocrystal 2*.

2.1.3. Electrosteric Stabilization

Electrosteric stabilization includes two general methods: (i) a combination of charges and nonionic hydrophilic polymers, and (ii) polyelectrolytes. Charges and nonionic hydrophilic polymers are applied to impose both electrostatic stabilization by the surface charges and steric stabilization by the nonionic hydrophilic polymers that dangle in the solution. Modification of this stabilization method for realizing oriented attachment would be the selective adsorption of both charges and polymers on all the crystallographic surfaces except those surfaces where oriented attachment is to occur. One typical example is the growth of pearl-like TiO_2 necklaces by functionalization of preformed TiO_2 nanoparticles of 5 nm with a ligand $(HOCH_2)_3CNH_2$.[144] $(HOCH_2)_3CNH_2$ molecules bind to all surfaces except (001) because of their preferential desorptions from (001) during reflux. The amino function is positively charged and imparts repulsive electrostatic force between adsorbed surfaces. The $(HOCH_2)_3$ introduces certain steric hindrance between

approaching nanopaticles. Consequently, these bound $(HOCH_2)_3CNH_2$ molecules direct the assembly of the functionalized TiO_2 nanoparticles along the [001] axis. Polyelectrolytes are ionic polymers which ionize in water to impose electrostatic stabilization and also dangle in water to act as steric barriers. Selective adsorption of polyelectrolytes on specific planes can also direct oriented attachment of nanocrystals. For example, poly(styrene-*alt*-maleic acid) molecules adsorb on "positively charged calcite (001) planes" leading to "surface stabilization and growth along *c*-axis direction".[145] This is shown in Figure 2 by the route *precursor ions & molecules -> nanocrystal 3 -> mesocrystal 6*.

2.2. Physical Fields

Apart from the interference of additives discussed above, inherent behavior such as the presence of electric dipoles and magnetic dipoles can also result in crystallographic alignment and thereby oriented attachment of the nanocrystalline subunits. Electron holography allows visualization of electric and magnetic nanofields around nanocrystals and reveals the presence of electric dipoles and magnetic dipoles.[146] The dipolar moment of nanocrystals can be strong enough to attract and orient with each other in the solution. For the cases where such dipolar interaction is nonexistent or not strong enough, external fields such as electric fields or magnetic fields can be applied to induce electric dipoles or magnetic dipoles and/or facilitate the crystallographic alignment process. In principle, if the

external fields are strong enough, the existent weak dipoles or induced dipoles respond to the external fields and rotate and move as directed by the external fields. The orientational growth process is driven by electrostatic or magnetostatic energy. However, it is noteworthy that the electric dipoles, magnetic dipoles, electric fields and magnetic fields have to be anisotropic with respect to the nanocrystals such that they can be aligned crystallographically.[4] These strategies can result in mesocrystals as shown by the two routes in Figure 1: *precursor ions -> nanocrystal -> mesocrystal 1* and *precursor ions -> nanocrystal -> mesocrystal 2*.

2.2.1. Electric Dipoles

Electric dipoles are known as the spontaneous dipoles in ferroelectric materials such as $BaTiO_3$ and $BiFeO_3$.[147] It is straightforward that directed aggregation of such nanocrystals is commonly observed.[110, 148] Electric dipoles can also be caused by alternating positively and negatively charged atomic layers. For example, the dipoles in PbSe arising from the noncentrosymmetric arrangement of Pb- and Se-terminated {111} facets,[149, 150] and in ZnO due to alternating Zn^{2+} and O^{2-} {0001} planes.[143] In theory, the electric field of each dipolar nanocrystal operates on adjacent dipolar nanocrystals and can lead to mutual alignment if their dipole moment is strong enough.[146, 151-156]

Experimentally, Klokkenburg *et al.* adopted cryogenic TEM technique to observe *in-situ* dipolar structures formed via oriented attachment of PbSe quantum dots

(Figure 4).[155] Wide angle electron diffraction pattern shows the 3D superstructure of 7.7 nm PbSe nanocrystals crystallographically oriented with noticeable misorientation. Talapin *et al.* studied the superlattice structures formed by nearly spherical PbS, PbSe, InAs, and α–Fe_2O_3 nanocrystals and argued that the hexagonal-close-packed (hcp) and simple hexagonal (sh) packing of the nanocrystals were due to dipole interaction.[153] The intuition came from the result that entropy-driven packing of hard spheres had been modeled to be fcc structure [157] and kinetically driven packing of hard spheres had been experimentally shown to be fcc structure or random hexagonal-close-packed (rhcp)[158]. Other dipolar quantum dot systems that have been reported to aggregate via oriented attachment include PbS[125], CdTe[159], CdSe[155, 160], and Pt_3Fe[161]. For ZnO, extensive publications have reported various structures, where there is dipolar interaction among the ZnO nanocrystals.[37-42, 47, 48, 52] Similar mechanisms have been reported for $BaCO_3$[162] and $BaTiO_3$[152, 163].

Certain organic molecules can also exhibit dipolar structures, for example, proteins such as gelatine and D, L-Alanine. Polar organic mesocrystals of D, L-Alanine wires were synthesized in the absence of certain additives.[164, 165, 166] Simon *et al.* suggested that a parallel orientation of triple-helical protein fibers of gelatine gave rise to parallel ordering of dipoles that orientates the growth of fluorapatite–gelatine composites.[146, 167]

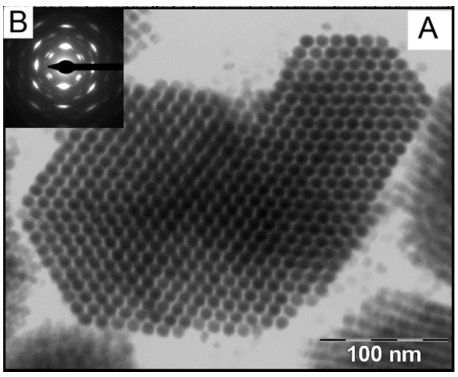

Figure 4. (A) TEM image showing a three-dimensional supercrystal formed by quasispherical PbSe nanocrystals of 7.7 nm. (B) wide-angle electron diffraction (WAED) pattern on one supercrystal, clearly illustrating atomic alignment. Adapted with permission from Ref. 155, Copyright 2007, American Chemical Society.

2.2.2. Magnetic Dipoles

Analogous to electric dipoles, magnetic dipoles can also direct the oriented attachment of certain magnetic nanocrystals and lead to the formation of crystallographically aligned structures. In theory, the magnetic field of each dipolar nanocrystals operates on adjacent dipolar nanocrystals and may cause mutual alignment if their dipole moment is strong enough.[168, 169] Experimentally, for example, strong magnetic dipolar interactions can help Fe_3O_4 ferrimagnetic nanocrystals of 53 nm to self-assemble into oriented 1D, 2D, and 3D superstructures in the absence of magnetic field (Figure 5).[170] Talapin *et al.*[153] and Rogach *et al.*[171] have reported that magnetic $CoPt_3$ nanocrystals could form hcp superlattice. Yao *et al.* reported self-assembly of hematite (α–Fe_2O_3) mesocrystals using a surfactant-free method and attributed the assembling process to its magnetic

property.[172]

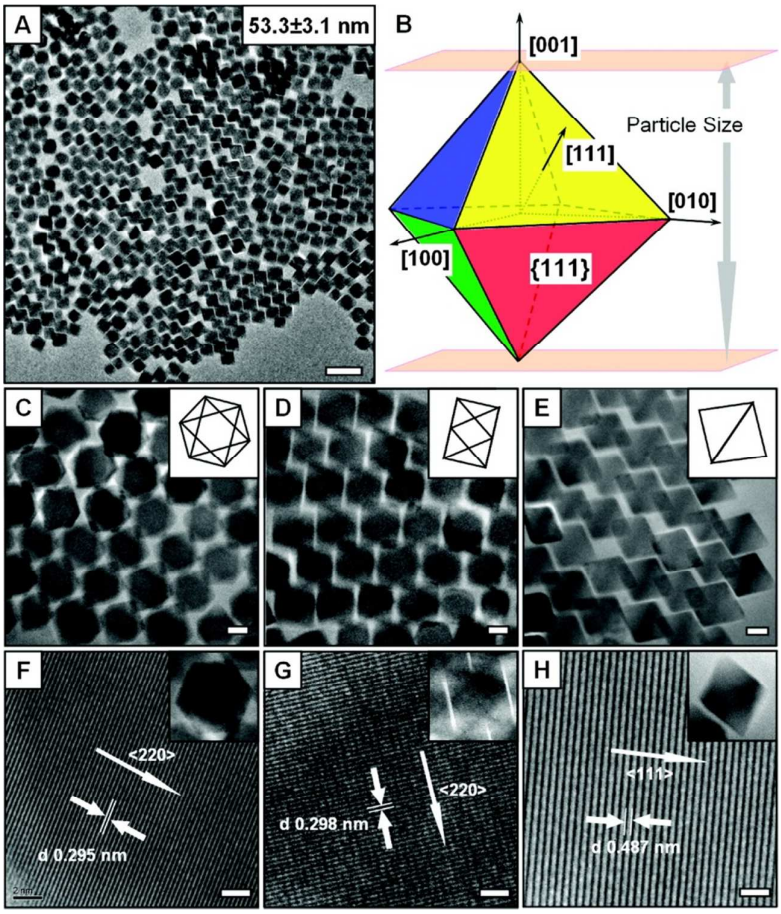

Figure 5. (A) TEM image of 53 nm Fe_3O_4 nanooctahedra. (B) Schematic 3D model of one octahedron-shaped nanoparticle. TEM and HRTEM images of 53 nm Fe_3O_4 nanooctahedra with different projection shapes: (C, F) hexagonal (zone axis: <111>), (D, G) rectangle (zone axis: <112>), and (E, H) parallelogram (zone axis: <110>). Scale bars: (A) 100 nm; (C–E) 20 nm; and (F–H) 2 nm. Reproduced with permission from Ref. 170, Copyright 2010, American Chemical Society.

2.2.3. Electric Field

Dipolar nanoparticles or anisotropically charged particles are responsive to external electric field. Therefore, external electric fields are able to impart extra

forces that affect the assembly process and consequently morphology of the resulted mesocrystals. Additionally, for non-dipolar nanocrystals, electric fields can induce polarization and thereby create dipoles in them. Theoretical works have been reported in literature.[173-175]

Experimentally, Ryan *et al.* applied an electric field of 1 V/μm to CdS nanorods (5 nm x 30 nm) dispersed in toluene to produce 2D and 3D assemblies of perpendicularly aligned nanorods on substrate.[176] Gupta *et al.* reported that alkane functionalized dipolar CdSe nanorods (8 nm x 40 nm) were able to stand perpendicular to substrate in correspondence to the applied external electric field of 10 V/μm, which was also perpendicular to the substrate.[177] Lausser *et al.* applied an external electric field of 0.1 V/μm to $BaTiO_3$ nanoparticles (< 50 nm) and the dipoles in different ferroelectric domains aligned with the direction of the electric field.[178] Their resultant superstructure was a "combined result of nanoparticle alignment by the electric field and crystallographic fusion of the nanoparticles under defined coincidence angles following an oriented attachment process".[178] Fang *et al.* prepared various shapes (rhombic hexahedron, cube and dodecahedron) and sizes (100 – 800 nm) of Ag_2O mesocrystals by adjusting the external electric field and growth time (Figure 6).[70]

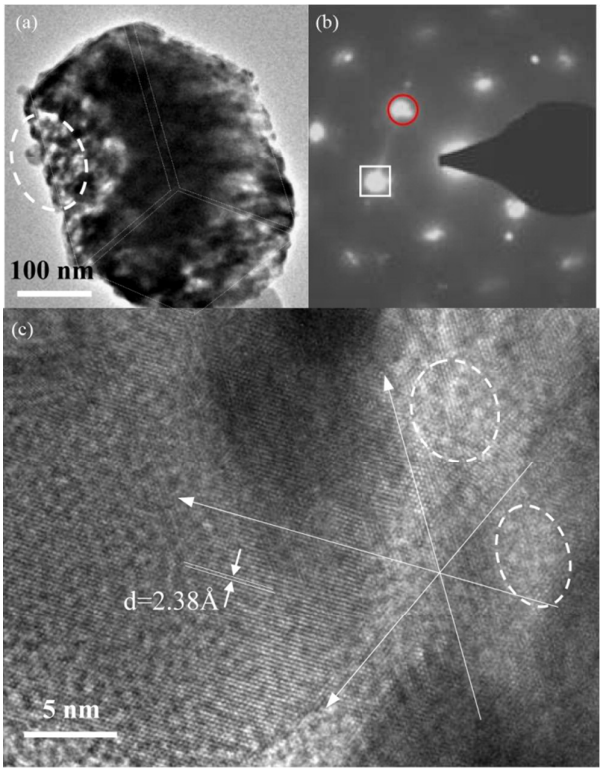

Figure 6. (a) TEM image of an Ag_2O mesocrystal synthesized at silver ion concentration of 1 mM, applied potential and growth time of 15 V @ 3 min. (b) SAED pattern obtained from the whole Ag_2O mesocube, indicating the single crystal-like nature. The circled and boxed spots in the SAED pattern are indexed as {1 1 1} and {2 0 0} Bragg reflections. (c) HRTEM image taken from the dashed circle area of Figure 6a. The white circles point to the mesopores and defects. Reproduced with permission from Ref. 70, Copyright 2010, Elsevier.

2.2.4. Magnetic Field

Externally applied magnetic fields are able to align the magnetic dipoles and consequently direct the oriented assembly of these nanocrystals. For the nanocrystals exhibiting no magnetic dipoles, such as superparamagnetic, paramagnetic and diamagnetic materials, externally applied magnetic fields are able to induce magnetic dipoles and the resultant interactions between magnetic dipoles

and the external magnetic field may align and assemble the nanocrystals in a crystallographic register. There have been theoretical works available in literature.[179-182] Experimental works are also widely reported as discussed below.

A systematic study done by Li *et al.* demonstrated that the strength of magnetic dipolar interaction fatally determines the ability for these nanocrystals to assemble into mesocrystals (Figure 7).[170] Such strength of magnetic dipolar interaction was manipulated by altering the size of Fe_3O_4 nanocrystals because magnetism is a volume dependent property that features the collective interaction of atomic magnetic dipoles. By applying a weak external magnetic field (around 0.06 T) the Fe_3O_4 nanocrystals of 21 nm self-assembled into crystallographically oriented superstructures. They successfully prepared 2D mesocrystals as large as 10 x 10 μm by applying the magnetic field horizontally with respect to the substrate. By changing the direction of magnetic field to perpendicular to the substrate 3D nanorod mesocrystals with 1.2 μm in length, 250 nm in diameter and long axis in [111] were obtained instead. However, when the magnetic dipolar interaction was too weak, mesocrystals could not form. For example, with the same external magnetic field the 8 nm Fe_3O_4 nanocrystals could not self-assemble into oriented superstructure due to the weak magnetic dipolar interaction. Similar results were also reported by Ahniyaz *et al.* that the formation of 3D mesocrystals of superparamagnetic Fe_3O_4 nanocrystals could be induced by modulation of the

magnetic dipolar interaction by means of a magnetic field.[183]

Various structures of cobalt have also formed *via* the oriented attachment of preformed nanocrystals due to directional attractive magnetic dipolar interaction under external magnetic field.[184, 185] Soumare *et al.* reported the formation of Ni nanofibers and nanowires of micrometer size, and demonstrated that the morphology of nanowires is dependent on the applied external magnetic field, *e.g.,* a smaller field (0.7 T) gave rise to Ni nanowires consisting of nanocrystals clearly observable under TEM, while a stronger field (1.4 T) gave rise to much smoother Ni nanowires.[186]

Diamagnets do not show magnetic dipoles by themselves but are able to create a magnetic field in opposition to an externally applied magnetic field. The resulted force may help the diamagnetic nanocrystals align with the magnetic field and form mesocrystals. Excellent examples include pseudo-single-crystallization of L-alanine and lysozyme by applying external magnetic fields.[180, 181, 187]

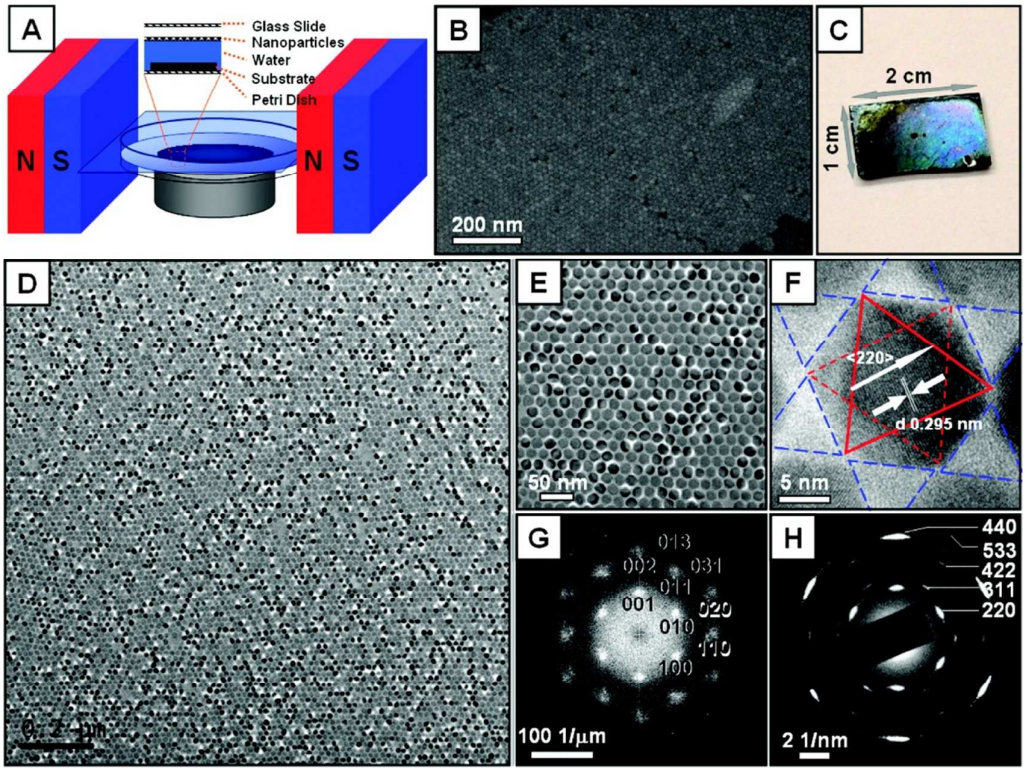

Figure 7. (A) Schematic illustration of the magnetic-field-induced assembly process. The toluene solution dispersed with 21 nm Fe_3O_4 nanooctahedra was carefully deposited on the water surface. After the solvent was evaporated off slowly in two days, the as-formed 2D monolayer was transferred onto solid substrates by lowering the water level carefully. (B) SEM image, (C) photograph, and (D–E) TEM images of the 2D monolayer assembly. (F) HRTEM TEM image of one single nanoparticle in the assembly (solid red triangle: (111) plane at the top; dashed red triangle: (111) plane at the bottom; solid blue triangles: interparticle spaces). Fast Fourier transformation (FFT) pattern (G) and selected area electron diffraction (SAED) pattern (H) of the 2D assembly corresponding to Figure 7E. Reproduced with permission from Ref. 170, Copyright 2010, American Chemical Society.

2.3. Organic Matrix

Composite structures consisting of organic matrix (*e.g.,* chitin) and inorganic materials (*e.g.,* $CaCO_3$) are commonly observed in nature. The organic matrix serves as both nucleation sites for the inorganic precursor ions and texture modifier

for the nucleated clusters.[188, 189] Almora-Barrios and Leeuw studied the nucleation of hydroxyapatite ($Ca_{10}(PO_4)_6(OH)_2$) on a collagen template by immersing triple-helical collagen in a stoichiometric solution of Ca^{2+}, PO_4^{3-}, and OH^- ions.[190] The formation of calcium phosphate clusters at the collagen template was initiated by the prevalent electrostatic attractions between Ca^{2+} and oxygen atoms of the glycine and hydroxyproline residues of collagen. Their simulations of collagen-surface interactions revealed that only the (0110) surface of hydroxyapatite interacted strongly with collagen peptides suggesting a growth-directing effect of the protein matrix. Similarly, Gehrke *et al.* could reproduce an artificial nacre structure that was comparable to natural nacre *via* mineralization formation on the residual matrix of natural nacre (Figure 8).[191] The residual matrix was prepared by demineralizing $CaCO_3$ in the natural nacre using 10% acetic acid. Mineralization formation on the residual matrix was carried out by placing it in a solution of calcium chloride, polyaspartic acid, and ammonium carbonate. Grassmann *et al.* prepared a composite structure consisting of polyacrylamide hydrogel and highly aligned calcite crystallites, a structure analogous to some biominerals.[192] The calcite aggregates were mineralized in the matrix resulting in an inorganic assembly intergrown with an organic hydrogel network. This route is shown in Figure 2 by *precursor ions & molecules -> mesocrystal 3*.

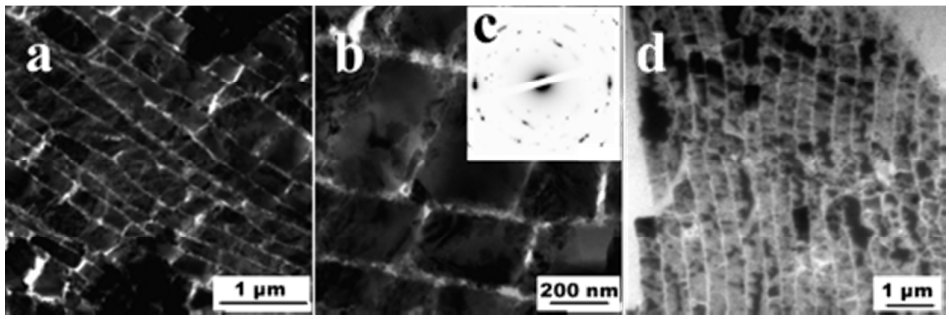

Figure 8. TEM micrographs of (a and b) of highly mineralized parts of synthetic nacre after 24 h reaction time. (c) Electron diffraction pattern of the platelets in panel b. (d) Original nacre from *Haliotis laevigata*. Reproduced with permission from Ref. 191, Copyright 2005, American Chemical Society.

2.4. Mineral Bridges

The building blocks in a mesocrystal can also be interconnected via mineral bridges so that integrity of the whole structure may be maintained. The mineral bridges appear straightforward to explain the mutual crystallographic orientation of the building blocks. Oaki *et al.* have observed similarly oriented architectures of bridged nanocrystals with incorporated polymers in both real biominerals (*e.g.,* shells, the sponge skeletons of echinoderms, a coral, a foraminifera, and eggshells of hens and emus) and their biomimetic architectures (*e.g.,*$CaCO_3$ synthesized in the presence of poly(acrylic acid), and re-mineralization of sea urchin spines) (Figure 9).[193] They proposed that formation of a mesocrystal with mineral bridges started with the formation of nanocrystals. Polymer adsorption onto the nanoparticles surface quenched its further growth. A site without the adsorption layer continued to grow through the adsorbed polymer layer forming the mineral

bridges that allowed growth of another nanocrystal. The process can be repeated until the mesocrystal is built up. Such a growth scenario is rather relevant for the mesocrystal formation within an amorphous precursor phase, which is commonly observed for biominerals and biomimetics. The bridges are also observed in other cases.[6, 194] This route is shown in Figure 2 by *precursor ions & molecules* -> *nanocrystal 2* -> *mesocrystal 5*.

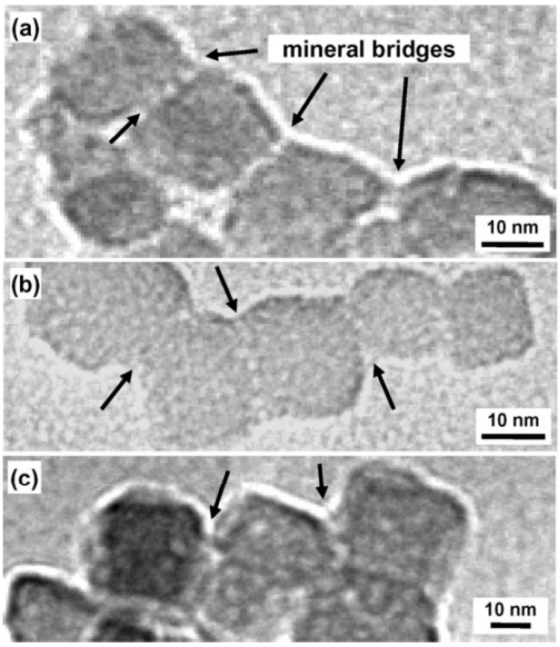

Figure 9. The oriented architecture consisting of bridged nanocrystals with incorporated biopolymers. The TEM images of the mineral bridges in sea urchin spines (a) and eggshells (b,c). Adapted with permission from Ref. 193, Copyright 2006, John Wiley and Sons.

2.5. Topotactic and Topochemical Reactions

Further reaction of a single crystal or mesocrystal may result in shrinkage of the unit cell and consequently give rise to a mesocrystal of another mineral system.

Zhou *et al.* reported that thermal treatment or boric acid treatment could convert NH_4TiOF_3 mesocrystals to TiO_2 mesocrystals (Figure 10).[137, 195] During the topotactic reaction, nitrogen, hydrogen, and fluoride atoms were removed and the resultant unit cell structure shrunk. Feng *et al.* also reported that NH_4TiOF_3 mesocrystals could be converted to TiO_2 mesocrystals via thermal treatment.[196] Wang *et al.* successfully applied the concept of topotactic reaction to achieving preferential growth and ordered arrangement of TiO_2 nanorods from $TiOF_2$ nanocubes.[197] This route is shown in Figure 1 by *single crystal -> mesocrystal 2*.

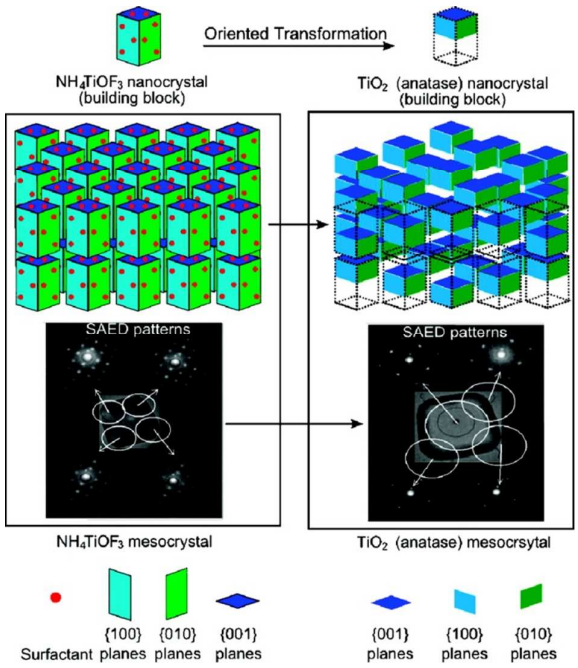

Figure 10. Illustration of the oriented transformation of NH_4TiOF_3 mesocrsytal to TiO_2 (anatase) mesocrystal. Reproduced with permission from Ref. 137, Copyright 2008, American Chemical Society.

2.6. Multiple Mechanisms and Stability of Nanocrystals

It is possible that more than one formation mechanisms can take effect in the same system. As an example, there may well be two formation mechanisms for NH_4TiOF_3 mesocrystals, namely, hydrophobic interparticle force and electric dipoles. Moreover, the stability, i.e., colloidal stability and chemical stability of the building blocks, is important for the successful development of mesocrystals.

Zhou *et al.* successfully developed NH_4TiOF_3 mesocrystals using a titanium precursor $(NH_4)_2TiF_6$, in combination with F-scavenger boric acid (H_3BO_3) and surfactant Brij 58 ($C_{16}H_{33}(OCH_2CH_2)_{20}OH$) in an aqueous solution at 35°C.[137, 195, 198] Selected area diffraction patterns (SAEDs) at different areas of one individual mesocrystal shows that NH_4TiOF_3 is single-crystal-like. A tentative mechanism was proposed, based on three steps: phase separation, matrix-mediated mesophase transformation and self-assembly of the building blocks into mesocrystals.[137, 198] In the first step, titanium precursor ions interact with the PEO groups (-$(OCH_2CH_2)_{20}$-) and condense leading to the formation of a viscous phase rich in surfactant. In the second step, the viscous phase undergoes a cooperative reorganization of inorganic and organic components and the surfactant matrix induced oriented crystallization leading to primary "square" building blocks. In the last step, the square building blocks self-assemble in a crystallographic register and form the final mesocrystals. The building blocks self-assemble because the Brij 58 molecules adsorb on their

surfaces *via* the PEO groups while the hydrophobic $C_{16}H_{33}$ groups interact to induce their mesoscale assembly. When the building blocks fuse, the adsorbed surfactant molecules leave the inorganic material and are restored to the aqueous solution, except that some surfactant molecules are occluded in the resultant mesocrystals. Elemental analysis revealed that the products contained impurities: carbon and boron.[137] Although the authors did not specify on the details why the building blocks, adsorbed by Brij 58 molecules on all surfaces, could assemble in an oriented manner, according to these authors, the mesoscale assembly process that takes place in the third step follows the route shown in Figure 2 by *precursor ions & molecules -> nanocrystal 1 -> mesocrystal 4*.

However, in the absence of hydrophobic interaction imposed by surfactant molecules, NH_4TiOF_3 mesocrystals can also form under various conditions. Lee and Shih prepared NH_4TiOF_3 "discoid crystals" on glass substrates at 40˚C for 2 h with the mixture of aqueous solutions of H_3BO_3 and $(NH_4)_2TiF_6$.[199] The NH_4TiOF_3 "discoid crystals" show single crystal diffraction patterns under TEM. Yu *et al.* synthesized NH_4TiOF_3 mesocrystals from H_3BO_3 and $(NH_4)_2TiF_6$ in a mixture of 2-propanol and water at 80 ˚C for 20 h by hydrothermal method.[200] Feng *et al.* obtained NH_4TiOF_3 mesocrystals from $TiCl_4$ and NH_4F in a mixture of water and ethanol or propanol at 180 ˚C for 12 h by hydrothermal method.[201] The research group of Zhou *et al.* also reported that by replacing Brij 58 surfactant with PEG

($H–(OCH_2CH_2)_n–OH$) (MW 1000, 10000 and 20000) NH_4TiOF_3 mesocrystals could be developed without providing the necessary reason for mesoscale assembly.[80] Our research group also observed that, instead of Brij 58, the addition of ethanol, ethylene glycol, diethylene glycol, or PEG MW 200 also gave rise to formation of NH_4TiOF_3 mesocrystals in the mixed aqueous solutions of H_3BO_3 and $(NH_4)_2TiF_6$ (Figure 11a, b).[81] Therefore, it is apparent that NH_4TiOF_3 tends to grow *via* the route of mesocrystals without necessary relation to the surfactant molecules introduced or precursors used.

In consideration of the previously discussed formation mechanisms of mesocrystals, it is speculated that this tendency of forming NH_4TiOF_3 mesocrystals must be related to the intrinsic properties of NH_4TiOF_3. Subsequently, we discovered ferroelectricity in NH_4TiOF_3 by piezoresponse force microscopy (PFM) technique (Figure 11c, d, e).[81] The first principles calculations also showed that NH_4TiOF_3 has a layered structure and the energetics favor a ferroelectric ground state with a polarization of 8 $\mu C/cm^2$.[81] The electric dipoles existent in NH_4TiOF_3 is able to induce the formation of NH_4TiOF_3 mesocrystals, as described in Section 2.2.1, in accordance with the route shown in Figure 1 *precursor ions -> nanocrystal -> mesocrystal 2*. It is useful for explaining formation of NH_4TiOF_3 mesocrystals in the absence of hydrophobic forces imposed by surfactant molecules.

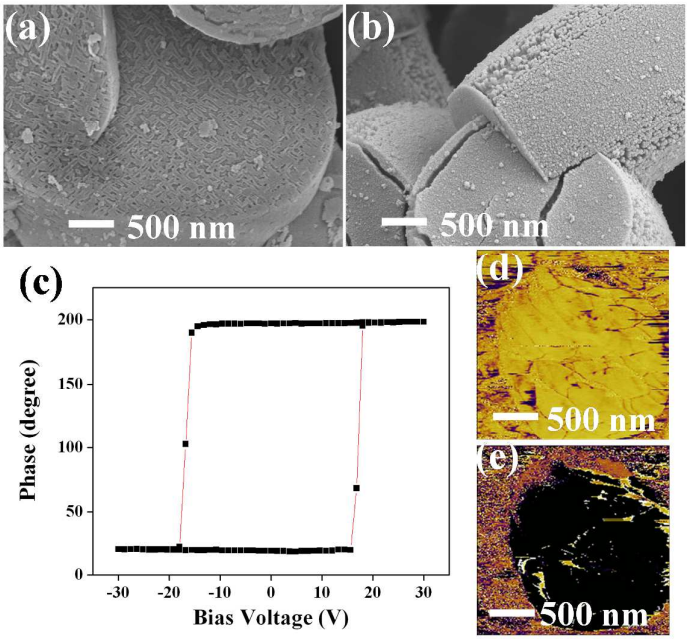

Figure 11. NH_4TiOF_3 mesocrystals are successfully synthesized with: (a) polyethylene glycol (PEG, MW 200) (10 wt%), and (b) diethylene glycol (DEG) (30 wt%). The individual NH_4TiOF_3 building blocks are clearly observed. The ferroelectricity of NH_4TiOF_3 demonstrated by piezoresponse force microscopy (PFM) technique: (c) phase hysteresis loop; (d) phase response after +15 V bias application; (e) phase response after -15 V bias application. Adapted with permission from Ref. 81, Copyright 2013, AIP Publishing LLC.

In order to form NH_4TiOF_3 mesocrystals, the colloidal NH_4TiOF_3 nanocrystals must be destabilized. Attractive interparticle force was introduced by Brij 58 molecules via the hydrophobic $C_{16}H_{33}$ chains. The intrinsic attractive interparticle force is the electric dipole-dipole interaction. The latter could be accumulative such that the attractive interparticle force increases with mesocrystal size, and this could be the reason why NH_4TiOF_3 mesocrystals synthesized with PEG (MW 1000, 10000 and 20000) are much larger than those with Brij 58.[80] The time required for

mesoscale assembly is longer for weaker interparticle forces. For example, when the hydrophobic $C_{16}H_{33}$ chains of Brij 58 was replaced with much less hydrophobic PPO chains of F127, lots of individual NH_4TiOF_3 nanocrystals were observed instead of NH_4TiOF_3 mesocrystals.[202]

In order to develop NH_4TiOF_3 mesocrystals, chemical stability of NH_4TiOF_3 nanocrystals must be preserved. Our studies show that NH_4TiOF_3 is not a stable compound and may convert to anatase TiO_2 in aqueous solution.[77, 79, 202] Once the NH_4TiOF_3 nanocrystals are formed, they are subject to both formation of mesocrystals and chemical conversion to anatase TiO_2. The outcome is dependent on the competition between these two processes. If the attractive interparticle force between NH_4TiOF_3 nanocrystals is strong enough, NH_4TiOF_3 mesocrystals tend to form as the mesoscale assembly process appears relatively faster. This point has been demonstrated by comparing Brij 58 and F127 and controlling hydrophobic force by varying the concentration of F127.[202] If the chemical conversion process appears relatively faster, anatase TiO_2 will be obtained. In addition to boric acid[137], there are three factors that may also affect the speed of this chemical conversion process: pH value, temperature and the amount and chain length of adsorbed polymers. Increasing either reaction temperature or reaction solution pH value facilitates the chemical reaction between NH_4TiOF_3 and H_2O.[79, 202] Even without hydrophobic forces, NH_4TiOF_3 nanocrystals always assemble into mesocrystals at a

low temperature (4 ^{o}C) because the electric dipole-dipole interaction was given ample time to operate on the nanocrystals.[81] However, at the same low temperature (4 ^{o}C), even in the presence of hydrophobic forces, the addition of ammonia solution could convert the NH_4TiOF_3 nanocrystals to anatase TiO_2 and avoided formation of mesocrystals.[79] Organic molecules that adsorb onto the surfaces of NH_4TiOF_3 nanocrystals are able to prevent them from reacting with water molecules and thereby slow down the chemical reaction process. Generally, the higher concentration of such molecules gives rise to better coverage and therefore higher chance for mesocrystal formation.[203] Similarly, longer chains of these molecules is favorable for forming mesocrystals as they prefer to interact with the surfaces of nanocrystals rather than dispersing in the solution.[204]

3. Applications

Mesocrystals may find applications in adsorbent, photocatalysis, energy storage, gas sensing, and biomedical applications due to their structural features such as crystalline subunits, oriented subunit alignment, high porosity, and bridges between the comprising subunits. Recently, quite a number of works have been reported on their applications. Herein, we summarize the research development in the performance and applications of mesocrystals between 2010 and 2013. We also compare the performances of several selected mesocrystals with their nanocrystal, polycrystal and single-crystal counterparts.

3.1. Adsorbent

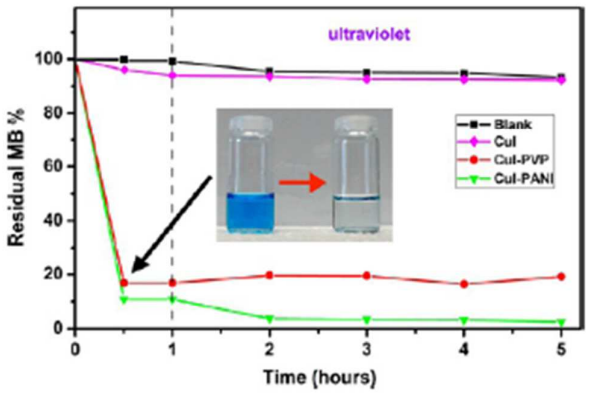

Figure 12. Adsorption rate of an aqueous solution of MB (4 mL, 6.4 g/L) for CuI-PVP and CuI-PANI mesocrystals, and for the as-received CuI powder. The mass of each sample was 10 mg. The photograph in the inset shows the color change of the MB solution before and 30 min after the addition of the CuI-PVP rods. Reproduced with permission from Ref. 109, Copyright 2013, American Chemical Society.

Kozhummal *et al.*[109] demonstrated that mesocrystals might serve as efficient adsorbents due to their large internal surface area derived from high porosity (Figure 12). For example, when 10 mg of CuI was dispersed in methylene blue (MB) (4 mL, 6.4 g/L) and stored in dark, after 30 min, CuI mesocrystals CuI-PVP and CuI-PANI could adsorb 83% and 90% of MB, respectively, while the as-received CuI powder showed negligible effect.

Zhou *et al.* also reported that the TiO_2 mesocrystals thermally converted from NH_4TiOF_3 at 700 ^oC showed a much higher adsorption capacity of MB molecules than polycrystals and nanocrystals (P25, Degussa) though it had the lowest specific surface area.[32] They attributed the high adsorption capacity to the high portion of

exposed {001} facets. The {001} facets have a high binding ability to water and thereby produces lots of •OH on the surfaces that are beneficial for adsorption capability. The 90 nm rod-like TiO_2 mesocrystals prepared by Li *et al.* also showed higher adsorption capacity for methylene orange than P25, as expected from its higher specific surface area (156 m^2/g vs 50 m^2/g).[18] Similar phenomenon for TiO_2 mesocrystals, in comparison to P25, has been reported by Yang *et al.*.[34]

3.2. Photocatalysis

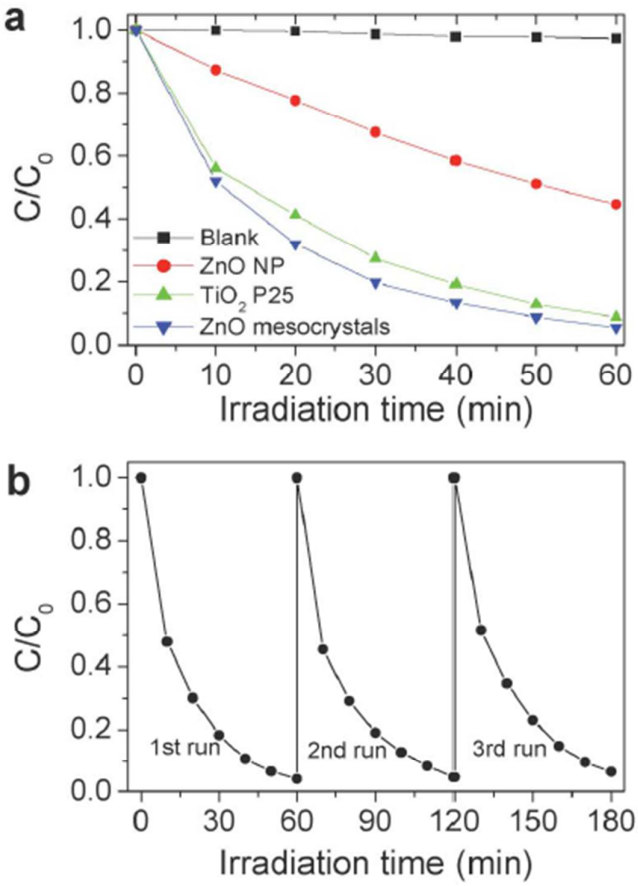

Figure 13. (a) Photocatalytic degradation of MB in the presence of various catalysts including ZnO mesocrystals under UV light irradiation; (b) recycled photocatalytic degradation of MB in the presence of ZnO mesocrystals under UV light irradiation. Reproduced from Ref. 205.

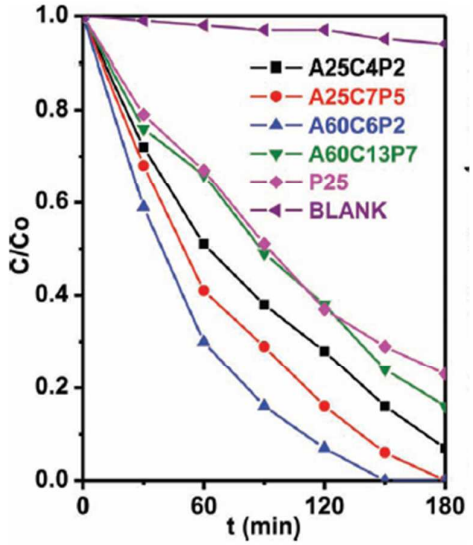

Figure 14. UV photocatalytic degradation (C/C_0 where C_0 is the initial concentration) of 2,4-dichlorophenol in the presence of different samples including mesocrystals P25. The figure includes a blank experiment (only 2,4- dichlorophenol) that shows no significant degradation when compared to the suspensions containing the different anatases. Reproduced with permission from Ref. 19, Copyright 2011, John Wiley and Sons.

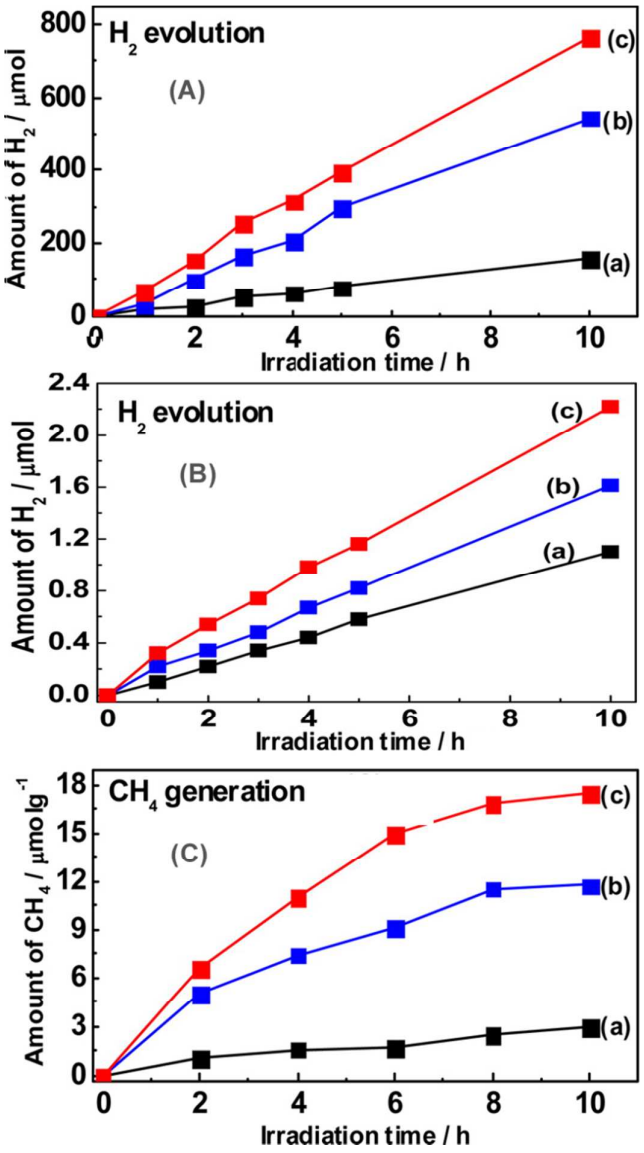

Figure 15. (A) Photocatalytic hydrogen evolution from 2 wt % Pt loaded photocatalysts in the presence of methanol as an electron donor; (B) Photocatalytic hydrogen evolution from bare photocatalysts without loading of cocatalyst in the presence of methanol as an electron donor to show that the variation in plot (A) comes from the materials rather than Pt loaded; (C) Photocatalytic reduction of CO_2 to CH_4 in the presence of water vapor from 1 wt % RuO_2 loaded photocatalysts: (a) solid and (b) hollow anatase TiO_2 single crystals, and (c) hollow anatase TiO_2 mesocrystals, with dominant {101}. Adapted with permission from Ref.22, Copyright 2012, American Chemical Society.

Several mesocrystals show highly interesting photocatalytic performance owing to their high levels of porosity, surface area, crystallinity, and exposure of the photocatalytically efficient facets. Specifically, the enhanced photocatalytic activity of mesocrystals can be attributed to several factors: (i) the long-lived reactive intermediates due to increased charge separation efficiency because of crystallographically aligned 3D crystalline network structure; (ii) abundant reaction sites for photocatalytic reactions due to the large specific surface area; (iii) faster reaction due to exposure of the photocatalytically efficient facets; (iv) efficient transportation of reagents and products due to high porosity; and (v) retaining high photocatalytic activity due to structural integrity, in comparison to decaying to photocatalytic activity of nanocrystals due to coagulation over time[206]. Interestingly, composite of graphene and TiO_2 mesocrystals demonstrates new direction for further tremendously enhancing photocatalytic activity probably due to large surface area, good flexibility, high electrical conductivity, and high chemical stability of graphene.[34] Summary of works in this area is shown in Table 1 and selected examples are briefly discussed below. It is noteworthy that very high photocatalytic activity can be achieved at very low surface areas suggesting the great promises of mesocrystals.[23, 31]

According to Wang *et al.*[205], ZnO mesocrystals were much more photocatalytically efficient than ZnO nanoparticles and even better than Degussa

P25 TiO_2 (Figure 13a). The superior efficiency in photocatalysis of the ZnO mesocrystals as compared to the ZnO nanoparticles was attributed to the photocatalytic activity of nonpolar $\{10\bar{1}0\}$ and polar {0001} surface. In addition, photocatalytic performance for the ZnO mesocrystals showed no apparent decrease throughout three catalytic cycles (Figure 13b).

Tartaj and Amarilla reported anatase mesocrystals (BET surfaces are above 150 $m^2\ g^{-1}$ with pore sizes above 4 nm) that showed superior photocatalytic performance to Degussa P25 TiO_2 for degrading 2,4-dichlorophenol under UV (Figure 14).[19] Their study suggests that active surface area and crystallinity are important parameters for controlling its performance.

Jiao *et al.* compared photocatalytic performances of solid anatase single crystals, hollow anatase single crystals and anatase mesocrystals with dominant reactive {101} facets using PO_4^{3-}/F^- as morphology controlling agent (Figure 15).[22] For H_2 evolution from water splitting and CH_4 generation from photoreduction of CO_2, they observed that anatase mesocrystals performed the best and solid anatase single crystals performed the worst, regardless of the presence of Pt loaded. The phenomenon was attributed to the synergistic effects of shortened bulk diffusion length of carriers and increased surface area. Bian *et al.* showed that anatase mesocrystals required much less noble metals to achieve the same yield for photodegrading 4-chlorophenol with various anatase nanoparticles.[207]

Table 1. Summary of mesocrystals applied as photocatalysts

mesocrystal	surface area (m^2 /g)	Pollutant/Purpose	Performance	Ref.
ZnO	-	methylene blue	>NP; >TiO_2 (P25)	205
ZnO	43	methylene blue	< TiO_2 (P25)	44
TiO_2	>150	2,4-dichlorophenol	>TiO_2 (P25)	19
TiO_2	42	H_2 & CH_4 production	>NP; >SC	22
TiO_2	63	4-chlorophenol	>NP	207
TiO_2	6.7	methylene blue	>PC; >TiO_2 (P25)	32
TiO_2	19	styrene	>TiO_2 (P25)	31
TiO_2	85.3	methylene blue; H_2 production	-	33
TiO_2	63	4-chlorophenol	>SC; >NP; >TiO_2 (P25)	29
TiO_2	155	methyl orange	>TiO_2 (P25)	18
TiO_2	57	rhodamine B	>TiO_2 (P25)	21
TiO_2	72	phenol	>TiO_2 (P25)	34
TiO_2	10	nitrosobenzene	>TiO_2 (P25)	23
TiO_2	36	Orange II	-	79
TiO_2	22	Orange II	-	202
$SrTiO_3$	21	H_2 production	-	115
$AgIn(WO_4)_2$	-	rhodamine B	< TiO_2 (P25)	106
$W_{18}O_{49}$	56	methyl orange	-	68
Fe_2O_3	29	rhodamine B	-	56
CuO	19.7	rhodamine B	>SC	66

NP denotes nanoparticle counterpart; SC denotes single-crystal counterpart; PC denotes polycrystal; > denotes higher photocatalytic activity than; < denotes lower photocatalytic activity than.

3.3. Energy Storage

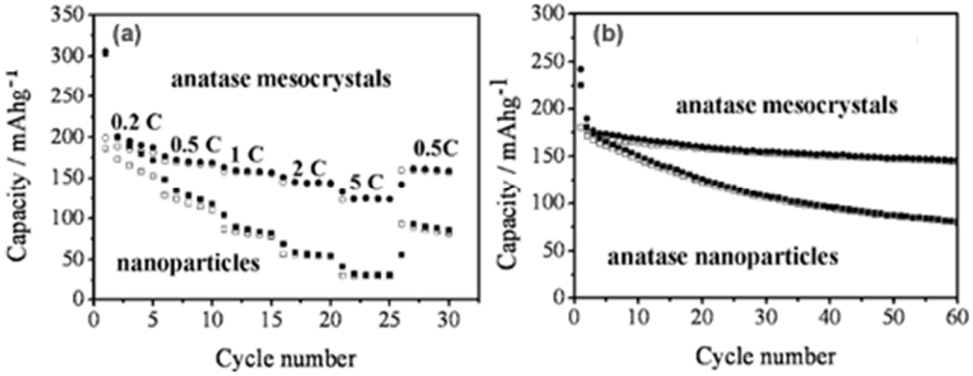

Figure 16. (a) rate capability of microporous anatase TiO_2 mesocrystals and anatase nanoparticles from 0.2 to 5 C, and (b) cycling performance of microporous anatase TiO_2 mesocrystals and anatase nanoparticles at a current rate of 1 C. Open symbols: discharge capacity; filled symbols: charge capacity. Adapted with permission from Ref. 24, Copyright 2012, John Wiley and Sons.

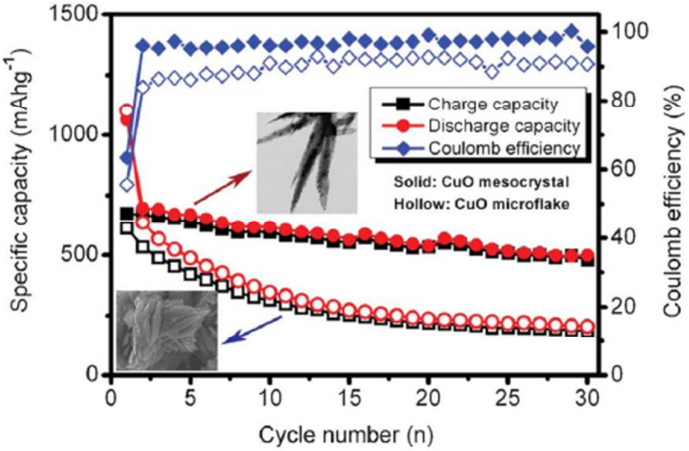

Figure 17. The cycle performance of the leaf-like CuO mesocrystal and CuO microflake. Reproduced from Ref.64.

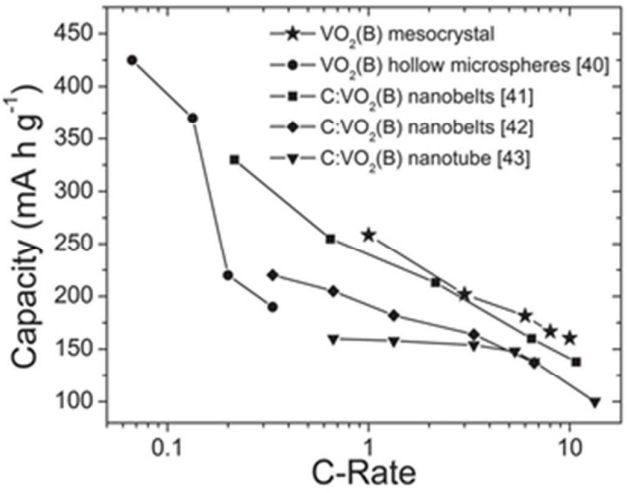

Figure 18. VO_2 mesocrystal in comparison with various VO_2(B) structures reported in literature (assuming a 1 C current density of 150 mA g^{-1}). Reproduced with permission from Ref.62, Copyright 2013, John Wiley and Sons.

Performance of electrode materials for lithium ion battery and supercapacitor can be improved using certain mesocrystals. Mesocrystals exhibit the level of porosity that can provide a fast channel of accessibility for the electrolyte and alleviate the effect of volume expansion during the intercalation/de-intercalation reactions. Since the consisting subunits are interconnected, charge transport is improved for mesocrystals in comparison to their nanoparticle counterparts. Furthermore, the high crystallinity of mesocrystals enhances charge separation and greatly reduces charge recombination. Summary of works for energy storage is shown in Table 2 and selected examples are briefly discussed below. Notably $LiFePO_4$ mesocrystals with a carbon coating delivered higher capacity in charge and discharge capacities and cyclic stability for lithium ion battery suggesting that composite of mesocrystal

may further improve the performance. [87, 88, 208]

Hong *et al.*[24] compared the rate capacity and cycling performances of anatase TiO_2 mesocrystals and nanoparticles of similar surface area (200 m^2g^{-1}) (Figure 16). According to their study, specific charge and discharge capacities of mesocrystals were higher and less current rate dependent than nanoparticles from 0.2 C to 5 C (Figure 16a). At current rate of 2 C, the anatase mesocrystals and nanoparticles delivered discharge capacities of 151 and 57 $mAhg^{-1}$, respectively. Furthermore, anatase mesocrystals also showed better cyclic stability after 60 cycles at 1 C (Figure 16b). Ye *et al.*[20] and Hong *et al.*[24] also reported that TiO_2 mesocrystals showed better rate capacity and cycling performance in comparison to the nanoparticle counterparts.

Duan *et al.*[54] compared cycling performances of α-Fe_2O_3 single crystals and mesocrystals as anodes at a current rate of 0.1 C and found the α-Fe_2O_3 mesocrystals exhibited superior cycle stability during cycling. After the common drop during the first 5 cycles, α-Fe_2O_3 mesocrystals showed fine stability and remained at 756 $mAhg^{-1}$ after 50 cycles with a very high Coulombic efficiency (~ 100%). The superior cycle stability was attributed to the porosity of mesocrystals.

Similarly, Xu *et al.*[64], Dang et *al.*[120], and Uchaker *et al.*[62] reported that mesocrystals were better performers for lithium ion battery application than their counterparts. In contrast to CuO microflakes, CuO mesocrystals delivered much

higher charge and discharge capacities, exhibited better cyclic stability, and showed higher Coulombic efficiency (Figure 17).[64] $LiMn_2O_4$ mesocrystals exhibited better cyclic stability than the nanoporous counterparts.[120] As for VO_2(B), mesocrystals could deliver higher charge and discharge capacities at current rates from 1 C to 10 C than the hollow microspheres, nanobelts and nanotubes (Figure 18).[62]

Table 2. Summary of mesocrystals applied as energy storage materials

mesocrystal	surface area (m^2 /g)	Conductivity agent (%)	Scan rate	Capacity / Capacitance	Cycle number	Retention rate (%)	Coulombic efficiency (%)	Ref.
TiO_2	180	10	1 C	230 mAh/g	-	-	-	19
TiO_2	114	10	1 C	165 mAh/g	60	74	100	20
TiO_2	13	10	1 C	249 mAh/g	100	97	~100	24
TiO_2	225	10	1 C	242 mAh/g	60	60	~100	24
TiO_2	39	10	1 C	298 mAh/g	100	57	-	27
TiO_2	136	10	1 C	312 mAh/g	100	49	-	30
VO_2(B),	28	12	0.9 C	258 mAh/g	50	76	-	62
$LiMn_2O_4$	-	20	0.6 C	98 mAh/g	100	87	-	120
CuO	23	20	-	1063 mAh/g	30	50	96	64
Fe_2O_3	34	10	0.1 C	1500 mAh/g	50	~55	~100	54
$LiFePO_4$	11	20	1 C	20 mAh/g	-	-	-	208
$LiCoO_2$	-	10	1 C	150 mAh/g	50	80	-	104
$Co(OH)_2$	175	21	7.8 C	506 F/g	2000	97	99	122
$W_{18}O_{49}$	-	-	20 mV/s	579 F/g	-	-	-	67

3.4. Gas Sensing

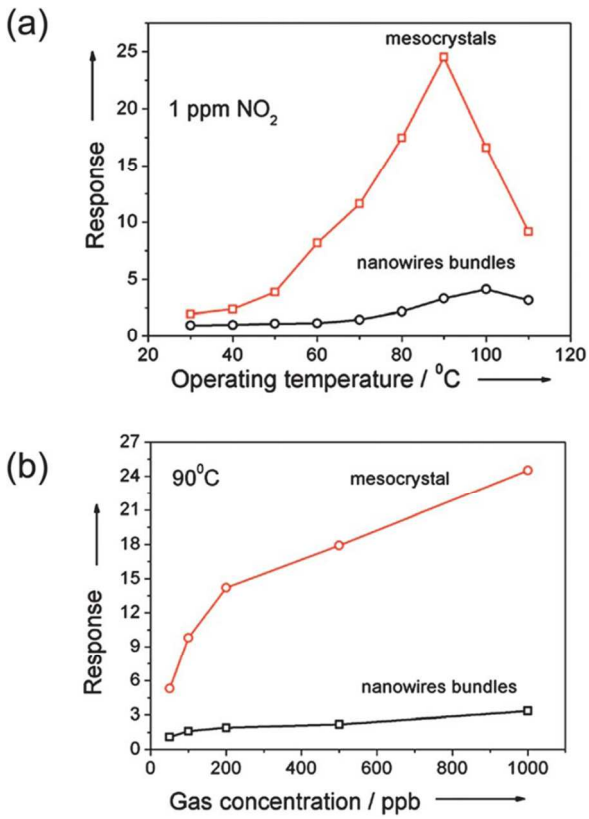

Figure 19. (a) Relationship between response and working temperature of mesocrystals (red line) and nanowires (black line) at different temperatures to 1 ppm of NO_2. (b) The response of mesocrystals (red line) and nanowires (black line) as a function of NO_2 gas concentration at 90 °C. The gas response is defined as the ratio between resistance R_g in gas and R_0 in air. Reproduced from Ref. 69.

The porous structure of mesocrystals also confers them favorable for gas sensing applications. Wang *et al.* prepared NO_2 gas sensors with $W_{18}O_{49}$ mesocrystals and nanowires of almost the same specific surface area.[69] For 1 ppm NO_2, the optimal working temperature of mesocrystals was 10 °C lower than that of nanowires and the

maximal response was 5 times higher than that of nanowires (Figure 19a). At an extremely low concentration of 50 ppb, the sensing response was 4 times higher than that of nanowires (Figure 19b). The sensing limit (saturation point) for high concentration for mesocrystals was expectantly higher than that for nanowires (Figure 19b). The authors attributed the superior performance of $W_{18}O_{49}$ mesocrystals over $W_{18}O_{49}$ nanowires to more oxygen vacancy sites associated with the porous structure. Liu *et al.* also reported much more superior gas (formaldehyde and ethanol) sensing property of Co_3O_4 mesocrystals in comparison to the commercially available powder counterparts.[58] Furthermore, the hybrid structure of Cu_2O mesocrystals and reduced graphene oxide (rGO) showed higher NO_2 gas sensitivity and lower detection limit at room temperature than the standalone counterparts Cu_2O mesocrystals and rGO (64 ppb, 81 ppb, and 82 ppb, respectively).[61] The synergistic effect of this hybrid structure, in comparison to Cu_2O mesocrystals alone, was attributed to further increased specific surface area and enhanced conductivity.

3.5. Biomedical Applications

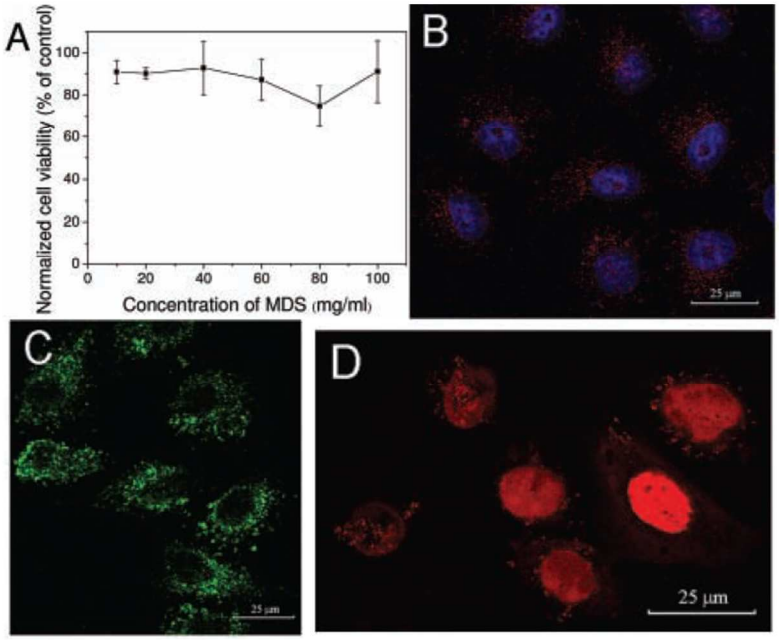

Figure 20. Application of $CaCO_3$ mesocrystals to drug delivery. (A) Cytotoxicity of the MDS (without DOX and pDNA) on HeLa cells for 12 h, ATTC CCL2. (B–D) Confocal laser scanning microscopy (CLSM) images for in vitro evaluation of the MDS containing DOX and pDNA on HeLa cells. (B) Cellular uptake of the MDS (with Au–DNA nanoparticles) for 4 h; merged image: cell nuclei were dyed blue by Hoechst 33258 and pDNA residues were dyed red by EtBr. (C) HeLa cells were transfected by the MDS (with Au–DNA nanoparticles). Green fluorescent protein (green) only exists in the cells successfully transfected by pDNA. (D) Cellular uptake of the MDS (with DOX) for 4 h; DOX shows as red dots. Adapted with permission from Ref. 209, Copyright 2010, John Wiley and Sons.

Mesocrystals have also been demonstrated for biomedical applications because their porosity may be used for incorporation and delivery of therapeutic agents. Zhao *et al.* developed a "multistage delivery system" (MDS) consisting of $CaCO_3$ mesocrystals as the biodegradable and biocompatible stage 1 microparticles (S1MPs) and the encapsulated Au nanoparticles as the stage 2 nanoparticles (S2NPs) with functional agents for biomedical applications (Figure 20).[209] The $CaCO_3$ mesocrystals were first

incorporated with superparamagnetic magnetite@silica nanoparticles so that the MDS could be concentrated at a specific site with the aid of an external magnetic field. Then a model drug, doxorubicin (DOX), was diffused into the porous $CaCO_3$ mesocrystals. Lastly, gene therapy was achieved by incorporating Au nanoparticles that were functionalized by plasmid of enhanced green fluorescent protein (pDNA). The co-delivery of DOX and Au-DNA nanoparticles by the $CaCO_3$ mesocrystals was verified on HeLa cells and A549 cells. The empty $CaCO_3$ mesocrystals were biocompatible as suggested by the low cytotoxicity (Figure 20a). Furthermore, DOX and DNA were successfully delivered into the cells to the right intracellular locations (Figure 20b-d).

4. Summary and outlook

Over the past several years, there have been around 50 compounds being reported for successful development of mesocrystals. While these recent works were largely concentrated on their synthesis and characterization, there have been studies for their potential applications. There are several different formation mechanisms reported for mesocrystals. Specifically, inspired by various colloidal techniques, the growth of mesocrystals can be modified by manipulating the interparticle forces, leading to oriented assembly of the colloidal nanoparticles and thereby steady formation of mesocrystals. Physical fields can strongly induce/manipulate the inherent responses of these colloidal nanoparticles and direct their oriented assembly. There have been investigations targeting the applications of mesocrystals, notably in five major areas:

adsorbent, photocatalysis, energy storage, gas sensing, and biomedical applications. The performance is largely determined by their mesocrystalline features, which can precede their nanocrystal, single-crystal, and polycrystal counterparts. Mesocrystals can be made to possess a high specific surface area, a controllable level of porosity, crystallinity in subunits, oriented subunit alignment, and the elegant 3D network structure. It would therefore be of interest to further develop synthesis strategies so that the most desirable mesocrystalline features are realized for targeted applications, for example, by fine tuning the existing synthesis strategies or establishing new ones. A few recent studies have demonstrated that hybrid structures of graphene and mesocrystal can give rise to better performances than the standalone mesocrystal counterparts in photocatalysis and energy storage applications. Another potential application area for these hybrid structures is for controlled drug release.

Acknowledgements

Authors acknowledge the supports of A*Star, Agency for Science, Technology and Research (Grants 1121480002 and 1121202013), and MOE Tier 2 (MOE2012-T2-2-102) Singapore, for research conducted at National University of Singapore.

References

(1) Petres, J. J.; Dezelic, G.; Tezak, B. *Croat. Chem. Acta* **1969,** *41*, 183-186.
(2) Cölfen, H.; Mann, S. *Angew. Chem. Int. Ed.* **2003,** *42*, 2350-2365.
(3) Cölfen, H.; Antonietti, M. *Angew. Chem. Int. Ed.* **2005,** *44*, 5576-5591.
(4) Song, R.-Q.; Cölfen, H. *Adv. Mater.* **2010,** *22*, 1301-1330.
(5) Li, H.; Estroff, L. A. *CrystEngComm* **2007,** *9*, 1153-1155.

(6) Inumaru, K. *Catal. Surv. Asia* **2006,** *10*, 151-160.
(7) You, H.; Ji, Y.; Wang, L.; Yang, S.; Yang, Z.; Fang, J.; Song, X.; Ding, B. *J. Mater. Chem.* **2012,** *22*, 1998-2006.
(8) Cao, Y.; Fan, J.; Bai, L.; Hu, P.; Yang, G.; Yuan, F.; Chen, Y. *CrystEngComm* **2010,** *12*, 3894-3899.
(9) Mondai, B.; Majumdar, D.; Saha, S. K. *J. Mater. Res.* **2010,** *25*, 383-390.
(10) Chen, F.; You, H.; Yang, S.; Yang, Z.; Song, X.; Lagally, M. G.; Ding, B. *Cryst. Growth Des.* **2011,** *11*, 3707-3712.
(11)Huang, X.; Tang, S.; Yang, J.; Tan, Y.; Zheng, N. *J. Am. Chem. Soc.* **2011,** *133*, 15946-15949.
(12) Lu, X.; Li, X.; Chen, F.; Ni, C.; Chen, Z. *J. Alloys Compd.* **2009,** *476*, 958-962.
(13) Wang, X.; Ma, Y.; Sugunan, A.; Qin, J.; Toprak, M.; Zhu, B.; Muhammed, M. *J. Nanopart. Res.* **2011,** *13*, 5879-5885.
(14) Wang, X.; Ma, Y.; Sugunan, A.; Qin, J.; Toprak, M. S.; Zhu, B.; Muhammed, M. *J. Nanopart. Res.* **2011,** *13*, 5879-5885.
(15) Xue, B.; Liu, R.; Xu, Z. D. *Materials Science and Engineering B: Solid-State Materials for Advanced Technology* **2011,** *176*, 210-216.
(16) Deng, W.; Wang, X.; Jiao, F.; Zhu, K. *J. Nanopart. Res.* **2013,** *15*, 1944-1953.
(17) Liu, S. J.; Gong, J. Y.; Hu, B.; Yu, S. H. *Cryst. Growth Des.* **2009,** *9*, 203-209.
(18) Li, L.; Liu, C. Y. *CrystEngComm* **2010,** *12*, 2073-2078.
(19) Tartaj, P.; Amarilla, J. M. *Adv. Mater.* **2011,** *23*, 4904-4907.
(20) Ye, J.; Liu, W.; Cai, J.; Chen, S.; Zhao, X.; Zhou, H.; Qi, L. *J. Am. Chem. Soc.* **2011,** *133*, 933-940.
(21) Da Silva, R. O.; Gonalves, R. H.; Stroppa, D. G.; Ramirez, A. J.; Leite, E. R. *Nanoscale* **2011,** *3*, 1910-1916.
(22) Jiao, W.; Wang, L.; Liu, G.; Lu, G. Q.; Cheng, H. M. *ACS Catalysis* **2012,** *2*, 1854-1859.
(23) Chen, Q.; Ma, W.; Chen, C.; Ji, H.; Zhao, J. *Chem.-Eur. J.* **2012,** *18*, 12584-12589.
(24) Hong, Z.; Xu, Y.; Liu, Y.; Wei, M. *Chem.-Eur. J.* **2012,** *18*, 10753-10760.
(25) Luo, L.; Hui, J.; Yu, Q.; Zhang, Z.; Jing, D.; Wang, P.; Yang, Y.; Wang, X. *CrystEngComm* **2012,** *14*, 7648-7655.
(26) Wang, H.; Liu, Y.; Liu, Z.; Xu, H.; Deng, Y.; Shen, H. *CrystEngComm* **2012,** *14*, 2278-2282.
(27) Hong, Z.; Wei, M.; Lan, T.; Jiang, L.; Cao, G. *Energy and Environmental Science* **2012,** *5*, 5408-5413.
(28) Cai, J.; Ye, J.; Chen, S.; Zhao, X.; Zhang, D.; Chen, S.; Ma, Y.; Jin, S.; Qi, L. *Energy and Environmental Science* **2012,** *5*, 7575-7581.
(29) Bian, Z.; Tachikawa, T.; Majima, T. *J. Phys. Chem. Lett.* **2012,** *3*, 1422-1427.
(30) Hong, Z.; Wei, M.; Lan, T.; Cao, G. *Nano Energy* **2012,** *1*, 466-471.

(31) Chen, J.; Li, G.; Zhang, H.; Liu, P.; Zhao, H.; An, T. *Catal. Today* **2013**, In Press.
(32) Zhou, L.; Zhou, L.; Chen, J.; Ji, C.; O'Brien, P. *CrystEngComm* **2013,** *15*, 5012-5015.
(33) Yao, X.; Liu, X.; Liu, T.; Wang, K.; Lu, L. *CrystEngComm* **2013,** *15*, 10246-10254.
(34) Yang, X.; Qin, J.; Li, Y.; Zhang, R.; Tang, H. *J. Hazard. Mater.* **2013,** *261*, 342-350.
(35) Distaso, M.; MačKović, M.; Spiecker, E.; Peukert, W. *Chem.-Eur. J.* **2012,** *18*, 13265-13268.
(36) Wang, H.; Xin, L.; Wang, H.; Yu, X.; Liu, Y.; Zhou, X.; Li, B. *RSC Advances* **2013,** *3*, 6538-6544.
(37) Li, Z.; Geßner, A.; Richters, J.-P.; Kalden, J.; Voss, T.; Kübel, C.; Taubert, A. *Adv. Mater.* **2008,** *20*, 1279-1285.
(38) Mo, M. S.; Lim, S. H.; Mai, Y. W.; Zheng, R. K.; Ringer, S. P. *Adv. Mater.* **2008,** *20*, 339-342.
(39) Liu, Z.; Wen, X. D.; Wu, X. L.; Gao, Y. J.; Chen, H. T.; Zhu, J.; Chu, P. K. *J. Am. Chem. Soc.* **2009,** *131*, 9405-9412.
(40) Sun, S.; Zhang, X.; Zhang, J.; Song, X.; Yang, Z. *Cryst. Growth Des.* **2012,** *12*, 2411-2418.
(41) Ye, F.; Peng, Y.; Guang-Yi, C.; Deng, B.; An-Wu, X. *J. Phys. Chem. C* **2009,** *113*, 10407-10415.
(42) Tseng, Y. H.; Lin, H. Y.; Liu, M. H.; Chen, Y. F.; Mou, C. Y. *J. Phys. Chem. C* **2009,** *113*, 18053-18061.
(43) Yan, Z.; Zhu, K.; Chen, W. P. *Journal of Nanoscience and Nanotechnology* **2009,** *9*, 6627-6630.
(44) Dong, J. Y.; Lin, W. H.; Hsu, Y. J.; Wong, D. S. H.; Lu, S. Y. *CrystEngComm* **2011,** *13*, 6218-6222.
(45) Li, H.; Zhang, Y.; Liu, H.; Wang, J. *J. Am. Ceram. Soc.* **2011,** *94*, 3267-3275.
(46) Luković Golić, D.; Branković, G.; Počuča Nešić, M.; Vojisavljević, K.; Rečnik, A.; Daneu, N.; Bernik, S.; Šćepanović, M.; Poleti, D.; Branković, Z. *Nanotechnology* **2011,** *22*, 395603-395611.
(47) Liu, M. H.; Tseng, Y. H.; Greer, H. F.; Zhou, W.; Mou, C. Y. *Chem.-Eur. J.* **2012,** *18*, 16104-16113.
(48) Waltz, F.; Wißmann, G.; Lippke, J.; Schneider, A. M.; Schwarz, H. C.; Feldhoff, A.; Eiden, S.; Behrens, P. *Cryst. Growth Des.* **2012,** *12*, 3066-3075.
(49) Zhu, G.; Liu, Y.; Ji, Z.; Bai, S.; Shen, X.; Xu, Z. *Mater. Chem. Phys.* **2012,** *132*, 1065-1070.
(50) Distaso, M.; Segets, D.; Wernet, R.; Taylor, R. K.; Peukert, W. *Nanoscale* **2012,** *4*, 864-873.
(51) Li, T.; Cao, Z.; You, H.; Xu, M.; Song, X.; Fang, J. *Chem. Phys. Lett.* **2013,** *555*, 154-158.
(52) Wang, S. S.; Xu, A. W. *CrystEngComm* **2013,** *15*, 376-381.

(53) Lin, W. H.; Chang, T. F. M.; Lu, Y. H.; Sato, T.; Sone, M.; Wei, K. H.; Hsu, Y. J. *J. Phys. Chem. C* **2013,** *117*, 25596-25603.
(54) Duan, X.; Mei, L.; Ma, J.; Li, Q.; Wang, T.; Zheng, W. *Chem. Commun.* **2012,** *48*, 12204-12206.
(55) Yao, R.; Cao, C. *RSC Advances* **2012,** *2*, 1979-1985.
(56) Cai, J.; Chen, S.; Hu, J.; Wang, Z.; Ma, Y.; Qi, L. *CrystEngComm* **2013,** *15*, 6284-6288.
(57) Yao, R.; Cao, C.; Bai, J. *CrystEngComm* **2013,** *15*, 3279-3283.
(58) Liu, Y.; Zhu, G.; Ge, B.; Zhou, H.; Yuan, A.; Shen, X. *CrystEngComm* **2012,** *14*, 6264-6270.
(59) Wang, F.; Lu, C.; Qin, Y.; Liang, C.; Zhao, M.; Yang, S.; Sun, Z.; Song, X. *J. Power Sources* **2013,** *235*, 67-73.
(60) Chen, C. J.; Chiang, R. K.; Wang, S. L. *CrystEngComm* **2013,** *15*, 9161-9169.
(61) Deng, S.; Tjoa, V.; Fan, H. M.; Tan, H. R.; Sayle, D. C.; Olivo, M.; Mhaisalkar, S.; Wei, J.; Sow, C. H. *J. Am. Chem. Soc.* **2012,** *134*, 4905-4917.
(62) Uchaker, E.; Gu, M.; Zhou, N.; Li, Y.; Wang, C.; Cao, G. *Small* **2013,** *9*, 3880-3886.
(63) Zhao, J.; Tan, R.; Guo, Y.; Lu, Y.; Xu, W.; Song, W. *CrystEngComm* **2012,** *14*, 4575-4577.
(64) Xu, M.; Wang, F.; Ding, B.; Song, X.; Fang, J. *RSC Advances* **2012,** *2*, 2240-2243.
(65) Ikeda, T.; Oaki, Y.; Imai, H. *Chemistry - An Asian Journal* **2013**, 2064-2069.
(66) Sun, S.; Zhang, X.; Zhang, J.; Wang, L.; Song, X.; Yang, Z. *CrystEngComm* **2013,** *15*, 867-877.
(67) Wang, D.; Li, J.; Cao, X.; Pang, G.; Feng, S. *Chem. Commun.* **2010,** *46*, 7718-7720.
(68) Sun, S.; Chang, X.; Li, Z. *Mater. Charact.* **2012,** *73*, 130-136.
(69) Wang, D.; Sun, J.; Cao, X.; Zhu, Y.; Wang, Q.; Wang, G.; Han, Y.; Lu, G.; Pang, G.; Feng, S. *Journal of Materials Chemistry A* **2013,** *1*, 8653-8657.
(70) Fang, J.; Leufke, P. M.; Kruk, R.; Wang, D.; Scherer, T.; Hahn, H. *Nano Today* **2010,** *5*, 175-182.
(71) Suchanek, W. L.; Garcés, J. M. *CrystEngComm* **2010,** *12*, 2996-3002.
(72) Lausser, C.; Cölfen, H.; Antonietti, M. *ACS Nano* **2011,** *5*, 107-114.
(73) Zheng, M.; Liu, Y.; Xiao, Y.; Dong, H.; Feng, H.; Zhang, H.; Lei, B. *ACS Applied Materials and Interfaces* **2013,** *5*, 12561-12570.
(74) Lausser, C.; Kumke, M. U.; Antonietti, M.; Cölfen, H. *Z. Anorg. Allg. Chem.* **2010,** *636*, 1925-1930.
(75) Zhong, S. L.; Lu, Y.; Gao, M. R.; Liu, S. J.; Peng, J.; Zhang, L. C.; Yu, S. H. *Chem.-Eur. J.* **2012,** *18*, 5222-5231.
(76) Chen, S.; Zhang, L.; Wu, Y.; Zhou, G.; Liu, P.; Yang, Y.; Wang, S. *Mater. Lett.* **2013,** *106*, 326-331.
(77) Liu, Y.; Zhang, Y.; Tan, H.; Wang, J. *Cryst. Growth Des.* **2011,** *11*, 2905-2912.

(78) Liu, Y.; Zhang, Y.; Wang, J. *CrystEngComm* **2013,** *15*, 791-801.
(79) Liu, Y.; Zhang, Y.; Li, H.; Wang, J. *Cryst. Growth Des.* **2012,** *12*, 2625-2633.
(80) Inoguchi, M.; Afzaal, M.; Tanaka, N.; O'Brien, P. *J. Mater. Chem.* **2012**, 25123-25129.
(81) Liu, Y.; Kumar, A.; Fan, Z.; Zhang, Y.; Ke, Q.; Zeng, K.; Wang, J.; Singh, D. J.; Ong, K. P. *Appl. Phys. Lett.* **2013,** *102*, 232903-232905.
(82) Zhuang, J.; Yang, X.; Fu, J.; Liang, C.; Wu, M.; Wang, J.; Su, Q. *Cryst. Growth Des.* **2013,** *13*, 2292-2297.
(83) Wang, G.; Selbach, S. M.; Yu, Y.; Zhang, X.; Grande, T.; Einarsrud, M. A. *CrystEngComm* **2009,** *11*, 1958-1963.
(84) Bilecka, I.; Hintennach, A.; Djerdj, I.; Novák, P.; Niederberger, M. *J. Mater. Chem.* **2009,** *19*, 5125-5128.
(85) Uchiyama, H.; Imai, H. *Cryst. Growth Des.* **2010,** *10*, 1777-1781.
(86) Popovic, J.; Demir-Cakan, R.; Tornow, J.; Morcrette, M.; Su, D. S.; Schlögl, R.; Antonietti, M.; Titirici, M. M. *Small* **2011,** *7*, 1127-1135.
(87) Zhou, N.; Wang, H. Y.; Uchaker, E.; Zhang, M.; Liu, S. Q.; Liu, Y. N.; Cao, G. *J. Power Sources* **2013,** *239*, 103-110.
(88) Zhou, N.; Uchaker, E.; Wang, H. Y.; Zhang, M.; Liu, S. Q.; Liu, Y. N.; Wu, X.; Cao, G.; Li, H. *RSC Advances* **2013,** *3*, 19366-19374.
(89) Song, R. Q.; Xu, A. W.; Antonietti, M.; Cölfen, H. *Angew. Chem. Int. Ed.* **2009,** *48*, 395-399.
(90) Chen, L.; Shen, Y.; Xie, A.; Huang, B.; Jia, R.; Guo, R.; Tang, W. *Cryst. Growth Des.* **2009,** *9*, 743-754.
(91) Zhu, Y.; Liu, Y.; Ruan, Q.; Zeng, Y.; Xiao, J.; Liu, Z.; Cheng, L.; Xu, F.; Zhang, L. *J. Phys. Chem. C* **2009,** *113*, 6584-6588.
(92) You, C.; Zhang, Q.; Jiao, Q.; Fu, Z. *Cryst. Growth Des.* **2009,** *9*, 4720-4724.
(93) Song, R. Q.; Cölfen, H.; Xu, A. W.; Hartmann, J.; Antonietti, M. *ACS Nano* **2009,** *3*, 1966-1978.
(94) Li, W.; Wu, P. *CrystEngComm* **2009,** *11*, 2466-2474.
(95) Zhou, G. T.; Guan, Y. B.; Yao, Q. Z.; Fu, S. Q. *Chem. Geol.* **2010,** *279*, 63-72.
(96) Geng, X.; Liu, L.; Jiang, J.; Yu, S. H. *Cryst. Growth Des.* **2010,** *10*, 3448-3453.
(97) Gilbert, P. U. P. A.; Young, A.; Coppersmith, S. N. *Proc. Natl. Acad. Sci. U. S. A.* **2011,** *108*, 11350-11355.
(98) Benzerara, K.; Menguy, N.; Obst, M.; Stolarski, J.; Mazur, M.; Tylisczak, T.; Brown Jr, G. E.; Meibom, A. *Ultramicroscopy* **2011,** *111*, 1268-1275.
(99) Oaki, Y.; Adachi, R.; Imai, H. *Polym. J.* **2012,** *44*, 612-619.
(100) Seto, J.; Ma, Y.; Davis, S. A.; Meldrum, F.; Gourrier, A.; Kim, Y. Y.; Schilde, U.; Sztucki, M.; Burghammer, M.; Maltsev, S.; Jäger, C.; Cölfen, H. *Proc. Natl. Acad. Sci. U. S. A.* **2012,** *109*, 3699-3704.
(101) Hu, M.; Jiang, J. S.; Ji, R. P.; Zeng, Y. *CrystEngComm* **2009,** *11*, 2257-2259.
(102) Hu, M.; Jiang, J. S.; Lin, C. C.; Zeng, Y. *CrystEngComm* **2010,** *12*,

2679-2683.
(103) Ming, H.; Torad, N. L. K.; Chiang, Y. D.; Wu, K. C. W.; Yamauchi, Y. *CrystEngComm* **2012,** *14*, 3387-3396.
(104) Nakajima, K.; Oaki, Y.; Imai, H. *ChemPlusChem* **2013,** *78*, 1379-1383.
(105) Hara, H.; Takeshita, S.; Isobe, T.; Nanai, Y.; Okuno, T.; Sawayama, T.; Niikura, S. *J. Alloys Compd.* **2013,** *577*, 320-326.
(106) Hu, B.; Wu, L. H.; Liu, S. J.; Yao, H. B.; Shi, H. Y.; Li, G. P.; Yu, S. H. *Chem. Commun.* **2010,** *46*, 2277-2279.
(107) Marques, V. S.; Cavalcante, L. S.; Sczancoski, J. C.; Alcântara, A. F. P.; Orlandi, M. O.; Moraes, E.; Longo, E.; Varela, J. A.; Siu Li, M.; Santos, M. R. M. C. *Cryst. Growth Des.* **2010,** *10*, 4752-4768.
(108) Homeijer, S. J.; Barrett, R. A.; Gower, L. B. *Cryst. Growth Des.* **2010,** *10*, 1040-1052.
(109) Kozhummal, R.; Yang, Y.; Güder, F.; Küçükbayrak, U. M.; Zacharias, M. *ACS Nano* **2013,** *7*, 2820-2828.
(110) Dang, F.; Kato, K.; Imai, H.; Wada, S.; Haneda, H.; Kuwabara, M. *CrystEngComm* **2010,** *12*, 3441-3444.
(111) Dang, F.; Kato, K.; Imai, H.; Wada, S.; Haneda, H.; Kuwabara, M. *Chem. Eng. J.* **2011,** *170*, 333-337.
(112) Zheng, H.; Zhu, K.; Wu, Q.; Liu, J.; Qiu, J. *J. Cryst. Growth* **2012**, 300-307.
(113) Kageyama, H.; Oaki, Y.; Takezawa, Y.; Suzuki, T.; Imai, H. *Nippon Seramikkusu Kyokai Gakujutsu Ronbunshi/Journal of the Ceramic Society of Japan* **2013,** *121*, 388-392.
(114) Kalyani, V.; Vasile, B. S.; Ianculescu, A.; Buscaglia, M. T.; Buscaglia, V.; Nanni, P. *Cryst. Growth Des.* **2012,** *12*, 4450-4456.
(115) Kuang, Q.; Yang, S. *ACS Applied Materials and Interfaces* **2013,** *5*, 3683-3690.
(116) Park, N. H.; Wang, Y.; Seo, W. S.; Dang, F.; Wan, C.; Koumoto, K. *CrystEngComm* **2013,** *15*, 679-685.
(117) Jones, F.; Radomirovic, T.; Ogden, M. I. *Cryst. Growth Des.* **2012,** *12*, 3057-3065.
(118) Baynton, A.; Ogden, M. I.; Raston, C. L.; Jones, F. *CrystEngComm* **2012,** *14*, 1057-1062.
(119) Revealed, I.; Yuwono, V. M.; Burrows, N. D.; Soltis, J. A.; Lee Penn, R. *J. Am. Chem. Soc.* **2010,** *132*, 2163-2165.
(120) Dang, F.; Hoshino, T.; Oaki, Y.; Hosono, E.; Zhou, H.; Imai, H. *Nanoscale* **2013,** *5*, 2352-2357.
(121) Nguyen, T. D.; Mrabet, D.; Vu, T. T. D.; Dinh, C. T.; Do, T. O. *CrystEngComm* **2011,** *13*, 1450-1460.
(122) Hou, L.; Yuan, C.; Yang, L.; Shen, L.; Zhang, F.; Zhang, X. *CrystEngComm* **2011,** *13*, 6130-6135.
(123) Cong, H. P.; Ren, X. C.; Yao, H. B.; Wang, P.; Cölfen, H.; Yu, S. H. *Adv. Mater.* **2012,** *24*, 1309-1315.
(124) Ashok, V. D.; De, S. K. *J. Phys. Chem. C* **2011,** *115*, 9382-9392.

(125) Querejeta-Fernández, A.; Hernández-Garrido, J. C.; Yang, H.; Zhou, Y.; Varela, A.; Parras, M.; Calvino-Gámez, J. J.; González-Calbet, J. M.; Green, P. F.; Kotov, N. A. *ACS Nano* **2012,** *6*, 3800-3812.
(126) Guan, M.; Zhu, G.; Shang, T.; Xu, Z.; Sun, J.; Zhou, Q. *CrystEngComm* **2012,** *14*, 6540-6547.
(127) Hu, D.; Kong, X.; Mori, K.; Tanaka, Y.; Shinagawa, K.; Feng, Q. *Inorg. Chem.* **2013,** *52*, 10542-10551.
(128) Liu, S. S.; Ma, D. K.; Zhang, Y. Q.; Cai, P.; Chen, X. A.; Huang, S. M. *CrystEngComm* **2012,** *14*, 2899-2905.
(129) Song, R. Q.; Cölfen, H. *CrystEngComm* **2011,** *13*, 1249-1276.
(130) Zhou, L.; O'Brien, P. *Small* **2008,** *4*, 1566-1574.
(131) Fang, J.; Ding, B.; Gleiter, H. *Chem. Soc. Rev.* **2011,** *40*, 5347-5360.
(132) Zhou, L.; O'Brien, P. *The Journal of Physical Chemistry Letters* **2012,** *3*, 620-628.
(133) Napper, D. H. *Polymeric stabilization of colloidal dispersions*. Academic Press: London, 1983; pp 8-15.
(134) Yu, S. H.; Cölfen, H.; Tauer, K.; Antonietti, M. *Nature Materials* **2005,** *4*, 51-55.
(135) Yu, S. H.; Cölfen, H.; Mastai, Y. *Journal of Nanoscience and Nanotechnology* **2004,** *4*, 291-298.
(136) Li, M.; Schnablegger, H.; Mann, S. *Nature* **1999,** *402*, 393-395.
(137) Zhou, L.; Smyth-Boyle, D.; O'Brien, P. *J. Am. Chem. Soc.* **2008,** *130*, 1309-1320.
(138) Feigin, R. I.; Napper, D. H. *J. Colloid Interface Sci.* **1980,** *75*, 525-541.
(139) Murphy, C. J.; Thompson, L. B.; Alkilany, A. M.; Sisco, P. N.; Boulos, S. P.; Sivapalan, S. T.; Yang, J. A.; Chernak, D. J.; Huang, J. *J. Phys. Chem. Lett.* **2010,** *1*, 2867-2875.
(140) Sun, Z.; Ni, W.; Yang, Z.; Kou, X.; Li, L.; Wang, J. *Small* **2008,** *4*, 1287-1292.
(141) Penn, R. L.; Banfield, J. F. *Geochim. Cosmochim. Acta* **1999,** *63*, 1549-1557.
(142) Pacholski, C.; Kornowski, A.; Weller, H. *Angew. Chem. Int. Ed.* **2002,** *41*, 1188-1191.
(143) Herng, T. S.; Kumar, A.; Ong, C. S.; Feng, Y. P.; Lu, Y. H.; Zeng, K. Y.; Ding, J. *Sci. Rep.* **2012,** *2*, 587.
(144) Polleux, J.; Pinna, N.; Antonietti, M.; Niederberger, M. *Adv. Mater.* **2004,** *16*, 436-439.
(145) Xu, A.-W.; Antonietti, M.; Yu, S.-H.; Cölfen, H. *Adv. Mater.* **2008,** *20*, 1333-1338.
(146) Simon, P.; Zahn, D.; Lichte, H.; Kniep, R. *Angew. Chem. Int. Ed.* **2006,** *45*, 1911-1915.
(147) McGilly, L.; Byrne, D.; Harnagea, C.; Schilling, A.; Gregg, J. *Journal of Materials Science* **2009,** *44*, 5197-5204.
(148) Dang, F.; Kato, K.; Imai, H.; Wada, S.; Haneda, H.; Kuwabara, M. *Ultrason.*

Sonochem. **2010,** *17*, 310-314.
(149) Cho, K.-S.; Talapin, D. V.; Gaschler, W.; Murray, C. B. *J. Am. Chem. Soc.* **2005,** *127*, 7140-7147.
(150) Fang, C.; van Huis, M. A.; Vanmaekelbergh, D. l.; Zandbergen, H. W. *ACS Nano* **2009,** *4*, 211-218.
(151) Li, L.-s.; Alivisatos, A. P. *Phys. Rev. Lett.* **2003,** *90*, 097402.
(152) Yasui, K.; Kato, K. *J. Phys. Chem. C* **2012,** *116*, 319-324.
(153) Talapin, D. V.; Shevchenko, E. V.; Murray, C. B.; Titov, A. V.; Král, P. *Nano Lett.* **2007,** *7*, 1213-1219.
(154) Zhang, X.; Zhang, Z.; Glotzer, S. C. *J. Phys. Chem. C* **2007,** *111*, 4132-4137.
(155) Klokkenburg, M.; Houtepen, A. J.; Koole, R.; de Folter, J. W. J.; Erné, B. H.; van Faassen, E.; Vanmaekelbergh, D. *Nano Lett.* **2007,** *7*, 2931-2936.
(156) Li, D.; Nielsen, M. H.; Lee, J. R. I.; Frandsen, C.; Banfield, J. F.; De Yoreo, J. J. *Science* **2012,** *336*, 1014-1018.
(157) Bolhuis, P. G.; Frenkel, D.; Mau, S.-C.; Huse, D. A. *Nature* **1997,** *388*, 235-236.
(158) Norris, D. J.; Arlinghaus, E. G.; Meng, L.; Heiny, R.; Scriven, L. E. *Adv. Mater.* **2004,** *16*, 1393-1399.
(159) Tang, Z.; Kotov, N. A.; Giersig, M. *Science* **2002,** *297*, 237-240.
(160) Pradhan, N.; Xu, H.; Peng, X. *Nano Lett.* **2006,** *6*, 720-724.
(161) Liao, H.-G.; Cui, L.; Whitelam, S.; Zheng, H. *Science* **2012,** *336*, 1011-1014.
(162) Yao, Q. Z.; Guan, Y. B.; Zhou, G. T.; Fu, S. Q. *Eur. J. Mineral.* **2012,** *24*, 519-526.
(163) Yasui, K.; Kato, K. *Proceedings of Meetings on Acoustics* **2012,** *15*, 045002-045008.
(164) Ma, Y.; Cölfeh, H.; Antonietti, M. *J. Phys. Chem. B* **2006,** *110*, 10822-10828.
(165) Medina, D. D.; Mastai, Y. *Cryst. Growth Des.* **2008,** *8*, 3646-3651.
(166) Hod, I.; Mastai, Y.; Medina, D. D. *CrystEngComm* **2011,** *13*, 502-509.
(167) Simon, P.; Rosseeva, E.; Buder, J.; Carrillo-Cabrera, W. G.; Kniep, R. *Adv. Funct. Mater.* **2009,** *19*, 3596-3603.
(168) Maurer, T.; Zighem, F.; Fang, W.; Ott, F.; Chaboussant, G.; Soumare, Y.; Atmane, K. A.; Piquemal, J.-Y.; Viau, G. *J. Appl. Phys.* **2011,** *110*, 123924-6.
(169) Awschalom, D. D.; DiVincenzo, D. P. *Physics Today* **1995,** *48*, 43-48.
(170) Li, L.; Yang, Y.; Ding, J.; Xue, J. *Chem. Mater.* **2010,** *22*, 3183-3191.
(171) Rogach, A. L.; Talapin, D. V.; Shevchenko, E. V.; Kornowski, A.; Haase, M.; Weller, H. *Adv. Funct. Mater.* **2002,** *12*, 653-664.
(172) Yao, R.; Cao, C. *RSC Advances* **2012,** *2*, 1979-1985.
(173) Zorn, M.; Tahir, M. N.; Bergmann, B.; Tremel, W.; Grigoriadis, C.; Floudas, G.; Zentel, R. *Macromol. Rapid Commun.* **2010,** *31*, 1101-1107.
(174) Harnack, O.; Pacholski, C.; Weller, H.; Yasuda, A.; Wessels, J. M. *Nano Lett.* **2003,** *3*, 1097-1101.

(175) Jiang, K.; Liu, W.; Wan, L.; Zhang, J. *Sensors and Actuators B: Chemical* **2008,** *134*, 79-88.
(176) Ryan, K. M.; Mastroianni, A.; Stancil, K. A.; Liu, H.; Alivisatos, A. P. *Nano Lett.* **2006,** *6*, 1479-1482.
(177) Gupta, S.; Zhang, Q.; Emrick, T.; Russell, T. P. *Nano Lett.* **2006,** *6*, 2066-2069.
(178) Lausser, C.; Zahn, D.; Cölfen, H. *J. Mater. Chem.* **2011,** *21*, 16978-16982.
(179) Sklute, E. C.; Eguchi, M.; Henderson, C. N.; Angelone, M. S.; Yennawar, H. P.; Mallouk, T. E. *J. Am. Chem. Soc.* **2011,** *133*, 1824-1831.
(180) Kimura, T.; Kimura, F.; Yoshino, M. *Langmuir* **2006,** *22*, 3464-3466.
(181) Matsumoto, K.; Kimura, F.; Tsukui, S.; Kimura, T. *Cryst. Growth Des.* **2011,** *11*, 945-948.
(182) Chantrell, R. W.; Bradbury, A.; Popplewell, J.; Charles, S. W. *J. Appl. Phys.* **1982,** *53*, 2742-2744.
(183) Ahniyaz, A.; Sakamoto, Y.; Bergström, L. *Proceedings of the National Academy of Sciences* **2007,** *104*, 17570-17574.
(184) Balela, M. D. L.; Yagi, S.; Matsubara, E. *Electrochem. Solid-State Lett.* **2011,** *14*, D68-D71.
(185) Legrand, J.; Ngo, A. T.; Petit, C.; Pileni, M. P. *Adv. Mater.* **2001,** *13*, 58-62.
(186) Soumare, Y.; Dakhlaoui-Omrani, A.; Schoenstein, F.; Mercone, S.; Viau, G.; Jouini, N. *Solid State Commun.* **2011,** *151*, 284-288.
(187) Kimura, F.; Mizutani, K.; Mikami, B.; Kimura, T. *Cryst. Growth Des.* **2011,** *11*, 12-15.
(188) Dey, A.; Bomans, P. H. H.; Müller, F. A.; Will, J.; Frederik, P. M.; de With, G.; Sommerdijk, N. A. J. M. *Nat Mater* **2010,** *9*, 1010-1014.
(189) Rauch, M. W.; Dressler, M.; Scheel, H.; Van Opdenbosch, D.; Zollfrank, C. *Eur. J. Inorg. Chem.* **2012**, 5192-5198.
(190) Almora-Barrios, N.; De Leeuw, N. H. *Cryst. Growth Des.* **2011,** *12*, 756-763.
(191) Gehrke, N.; Nassif, N.; Pinna, N.; Antonietti, M.; Gupta, H. S.; Cölfen, H. *Chem. Mater.* **2005,** *17*, 6514-6516.
(192) GRASSMANN, O.; NEDER, R. B.; PUTNIS, A.; LÖBMANN, P. *Am. Mineral.* **2003,** *88*, 647-652.
(193) Oaki, Y.; Kotachi, A.; Miura, T.; Imai, H. *Adv. Funct. Mater.* **2006,** *16*, 1633-1639.
(194) Miura, T.; Kotachi, A.; Oaki, Y.; Imai, H. *Cryst. Growth Des.* **2006,** *6*, 612-615.
(195) Zhou, L.; O'Brien, P. *Phys. Status Solidi A* **2008,** *205*, 2317-2323.
(196) Feng, J.; Yin, M.; Wang, Z.; Yan, S.; Wan, L.; Li, Z.; Zou, Z. *CrystEngComm* **2010,** *12*, 3425-3429.
(197) Wang, Z.; Huang, B.; Dai, Y.; Zhang, X.; Qin, X.; Li, Z.; Zheng, Z.; Cheng, H.; Guo, L. *CrystEngComm* **2012,** *14*, 4578-4581.
(198) Zhou, L.; Boyle, D. S.; O'Brien, P. *Chem. Commun.* **2007**, 144-146.
(199) Lee, M. K.; Shih, T. H. *J. Phys. D: Appl. Phys.* **2010,** *43*, 025402-025406.

(200) Yu, H.; Tian, B.; Zhang, J. *Chem.-Eur. J.* **2011,** *17*, 5499-5502.
(201) Feng, J.; Yin, M.; Wang, Z.; Yan, S.; Wan, L.; Li, Z.; Zou, Z. *CrystEngComm* **2010,** *12*, 3425-3429.
(202) Liu, Y.; Zhang, Y.; Wang, J. *CrystEngComm* **2013,** *15*, 791-801.
(203) Our unpublished data that no additive, EG (10%), EG (30%) at 23 ^{o}C for 3 days give rise to both NH_4TiOF_3 and TiO_2 for the first two formulations and only NH_4TiOF_3 for the last.
(204) Our unpublished data that PEG 200, 2000, 20000 (10%) at 23 ^{o}C for 3 days give rise to both NH_4TiOF_3 and TiO_2 for the first two formulations and only NH_4TiOF_3 for the last.
(205) Wang, M.; Zhang, Y.; Zhou, Y.; Yang, F.; Kim, E. J.; Hahn, S. H.; Seong, S. G. *CrystEngComm* **2013,** *15*, 754-763.
(206) Xiaowei, Z.; Limin, Q. *Nanotechnology* **2012,** *23*, 235604-235610.
(207) Bian, Z.; Tachikawa, T.; Kim, W.; Choi, W.; Majima, T. *J. Phys. Chem. C* **2012,** *116*, 25444-25453.
(208) Popovic, J.; Demir-Cakan, R.; Tornow, J.; Morcrette, M.; Su, D. S.; Schlögl, R.; Antonietti, M.; Titirici, M.-M. *Small* **2011,** *7*, 1127-1135.
(209) Zhao, Y.; Lu, Y.; Hu, Y.; Li, J. P.; Dong, L.; Lin, L. N.; Yu, S. H. *Small* **2010,** *6*, 2436-2442.